2020

Nanoscale modulation of friction and triboelectrification with application to electrohydrodynamic nanolithography

Qiang Li
Iowa State University

Nanoscale modulation of friction and triboelectrification with application to electrohydrodynamic nanolithography

by

Qiang Li

A dissertation submitted to the graduate faculty

in partial fulfillment of the requirements for the degree of

DOCTOR OF PHILOSOPHY

Major: Electrical Engineering (Microelectronics and Photonics)

Program of Study Committee:
Jaeyoun Kim, Co-major Professor
In Ho Cho, Co-major Professor
Rana Biswas
Meng Lu
Jiming Song

The student author, whose presentation of the scholarship herein was approved by the program of study committee, is solely responsible for the content of this dissertation. The Graduate College will ensure this dissertation is globally accessible and will not permit alterations after a degree is conferred.

Iowa State University

Ames, Iowa

2020

TABLE OF CONTENTS

Page

LIST OF FIGURES

ACKNOWLEDGMENTS

It's a great pleasure of embarking on this challenging but rewarding journey towards my Ph.D. degree in Electrical and Computer Engineering at Iowa State University. Now just steps away from the finish line, I would like to take this opportunity to thank all for their support, advice, and friendship during my six-year life and study in this great research community.

First and foremost, I would like express my sincere gratitude to my advisor, Prof. Jaeyoun Kim for his guidance, support, encouragement, and patience. It has been a great pleasure to work with him and I benefited a lot from his excellent teachings. I also want to thank my co-advisor, Prof. In Ho Cho, for his excellent knowledge in finite element analysis and machine learning, which make the multidisciplinary investigations possible.

I would like to appreciate the advisory and support from all my committee members. On most of work presented in this dissertation, we have been in close collaboration with Prof. Rana Biswas, who always provides insightful and inspiring guidance in our research meetings. Professor Jiming Song has provided great courses on electromagnetics and numerical simulations, which are widely used throughout this work and will also benefit my future career. Last but not least, I would like to thank Prof. Meng Lu for providing the semiconductors and microfabrication courses, and also his generosity of sharing lab facilities, like FTIR, UV-vis spectrometer.

The work in this dissertation would not be possible without the support from Dr. Wai Leung in Microelectronics Research Center on e-beam evaporator and contact aligner, Dr. Dapeng Jing and Dr. Warren Straszheim in the Material Analysis and Research Laboratory on scanning probe microscopy (SEM), and Dr. Eeshita Manna on atomic force microscopy (AFM). I also would like to thank Prof. Liang Dong and Prof. Long Que for sharing the lab facilities, like the wet bench, spectrometers, and digital micromirror device, without which this dissertation could have taken longer.

I would also like to express my gratitude to the great mentors in my early stage of study and research. It's a great pleasure to work with them. I would like to thank Dr. Jungwook Paek for the excellent tutoring about the soft-MEMS related fabrications, Dr. Rabin Dhakal for nanofabrications and soft-lithography, and Dr. Akshit Peer for plasmonics and functional metasurfaces. I also want to thank my lab colleague MyungGi Ji for his help in the experiment and manuscript revision.

I would like to acknowledge the funding support from National Science Foundation (CMMI-1265844, CBET-1605275, and CMMI-1760348) and William Catron Fellowship.

Finally, I wish to express my gratitude to my parents for their continuous encouragement and moral support.

ABSTRACT

Triboelectrification, or contact electrification (CE), is a common phenomenon in our daily life and has been studied for more than 2600 years, with its first observation dating back to the amber/wool rubbing experiment by Thales of Miletus. However, the underlying mechanism of CE remains elusive, although many researchers suggest the transfer of electrons, ions, or charged materials. Recently, CE is gaining popularity as a facile method to generate nanopatterned surface charge, with widespread applications in nanoxerography, thin film self-organization, and data storage. Of special interest is the CE induced by stamping nanotextured elastomer poly(dimethylsiloxane) (PDMS) masters onto the target surface because it can facilely achieve high-fidelity charge generation and nanopatterning thanks to the excellent flexibility of PDMS.

Here, we developed a simple charge patterning technique by replicating nanotextured molds with PDMS. It was found that the demolding action induced charges on the PDMS surface in a pattern closely correlated with the nanotexture. This new technique not only enables facile fabrication of nanoscale charge patterns on insulator surfaces but provide more specific targets for modeling and analysis of CE. By combining a variety of scanning probe microscopy technique (AFM/KPFM/EFM), electrostatic modeling, and finite element analysis (FEM), we developed a universal mechano-electric model than can explain how the generated nanopatterns are formed and affected by the interfacial nanotexture's morphology, as well as different material combinations. It turns out that the cumulative distance of the elastomer's tangential sliding during the interfacial separation plays the key role in shaping the charge distribution pattern. As an exemplary application, we configured the generated nanopatterned surface charge into a electrohydrodynamic lithography (EHDL) process, leading to nanovolcanos with 10 nm-scale craters. This EHDL process can be potentially used for fabricating functional material and metasurfaces.

CHAPTER 1. OVERVIEW

1.1 Introduction of Contact Electrification

Triboelectrification, or contact electrification (CE), is the generation of surface charge when two surfaces are brought into contact and separated [16, 17, 18]. The investigation dates back to more than 2600 years ago, with the report of amber charging against wool by Thales of Miletus [19]. It has been widely used in a variety of technologies such as electrostatic separation [20], electrophotography [21], and electrostatic trapping of nanometric objects [22]. However, the underlying mechanism remains elusive and the origin of the transferred charge carriers is still under debate [23, 24, 25], especially between insulators, due to the fact that their surface states are usually not well defined. It's commonly assumed that contact electrification requires a difference in the material properties and the gained surface charge distribution is spatially homogeneous [26, 27, 28].

Recently, contact electrification of elastomer surfaces has been attracting substantial interest, with the resulting tribocharges already playing crucial roles in energy harvesting [29, 30, 31], mass spectrometry [32], and electronics [33, 34]. It's demonstrated that CE can actually happen between identical materials [1, 35, 36]. In addition, the resulted surface charge distribution is not uniform, but a random "mosaic" of oppositely charged regions of nanoscopic dimensions [1], in contrast to the conventional picture of uniform charging.

As shown in Fig. 1.1, the conventional view assumes that after contact electrification, one surface is charged positively uniformly, while the other is charged negatively uniformly. However, the mosaic picture shows that both surfaces carry interleaved domains that are negatively and positively charged. With Kelvin probe force microscopy (KPFM) to measure the surface potential maps, it's found that the surfaces after contact electrification carry random "mosaic" of positively charged and negatively charged nanodomains. The working principle of KPFM and related technical details will be described in the next chapter. In addition, Fig. 1.2c shows that similar "mosaic" also

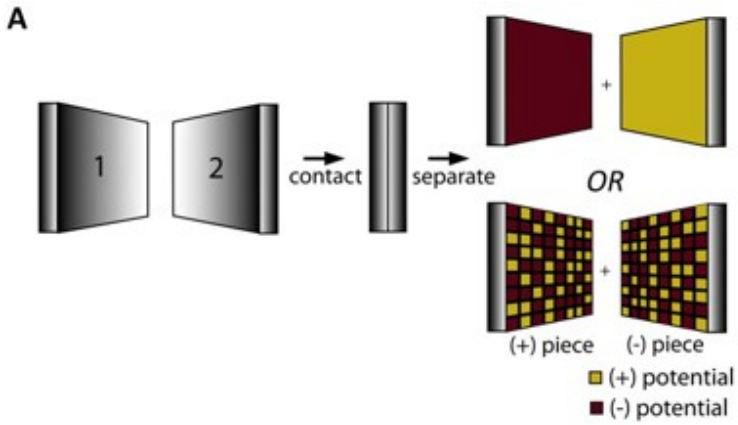

Figure 1.1 Scheme of the possible scenarios after contact electrification - two surfaces are uniformed charged with opposite signs of charge, or two surface both show negatively and positively charged nanodomains. Adapted from [1].

happens in the contact electrification between identical materials. Before the contact electrification, the pristine PDMS film or PC film were not charged, showing close to zero surface potential (Fig. 1.2b). After contacting with other materials, either the identical (PDMS-PDMS) or different material combinations (PDMS-PC), the potential maps consist of a mosaic of positive and negative regions. Further statistical analysis revealed that the mosaic is actually not pure random, but can be described as random scalar fields involving two length scales, one at several hundred nanometers and the other at tens of nanometers [1]. Similarly, identical polytetrafluoroethylene (PTFE) film were used to study the curvature effect during contact electrification [35].

Recently, a similar tribocharging has also been observed on the surface of the elastomer PDMS as the result of replica molding [37]. The ensuing studies revealed that the level of tribocharging is strong enough to influence some microfluidic functionalities, such as channel electrophoresis [38, 39, 40]. So far, however, this replica molding- induced tribocharging phenomenon has been studied only on flat, untextured elastomer surfaces. It is rather ironic since replica molding is the primary method for surface texturing of the PDMS. Questions regarding how those textures affect the tribocharge's generation and distribution patterns, especially at nanoscale, have been

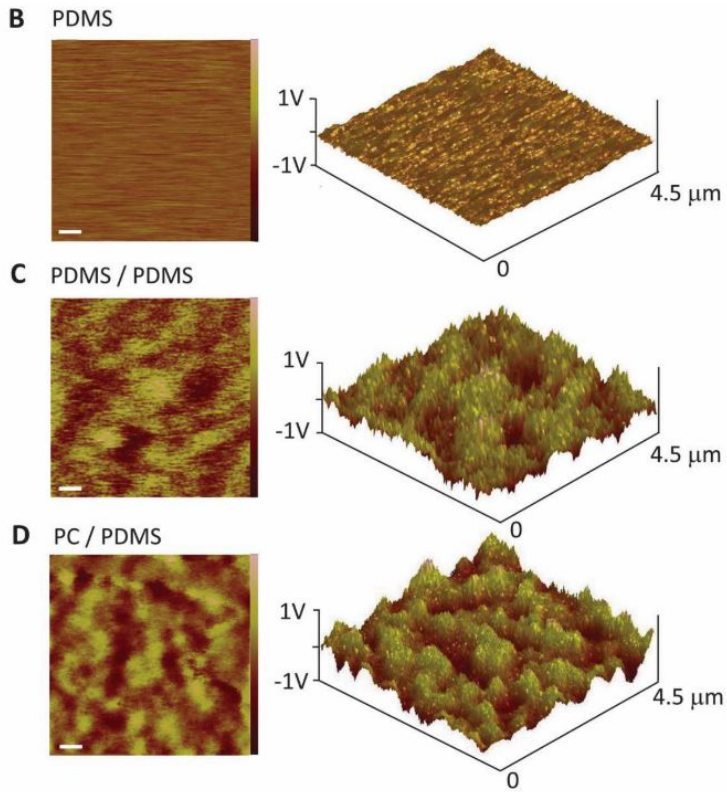

Figure 1.2 (b) Before contact electrification, the surface potential map is approximately uniform. (c) (d) However, the contact-charged surfaces features a mosaic of positive and negative nanodomains. More importantly, this contact electrification happens between not only different materials PDMS-PC, but also between identical material, PDMS-PDMS Adapted from [1].

left unanswered to date. This dissertation is devoted to answer these questions by combining multiphysical investigation techniques and establish new applications.

1.2 Nanopatterning of Surface Charge and Applications

Nanopatterning of tribocharge on material surface is playing an important role in many branches of nanotechnology, such as nanoxerography [41, 42], thin film self-organization [43], and data storage [44, 45]. A variety of techniques have been developed for its realization, falling into two main categories, scanning probe based direct writing and micro-contact printing. In direct writing-type techniques, the material surface is scanned with highly confined sources of electric charges such

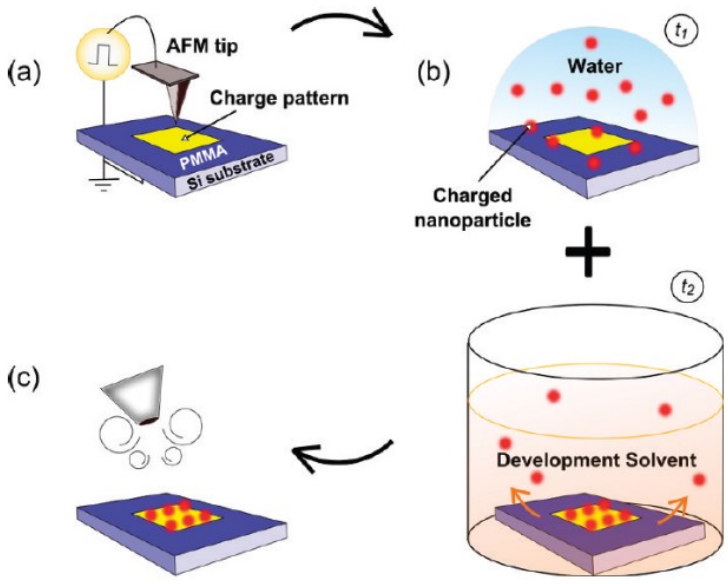

Figure 1.3 Schematics of contact mode AFM induced charge patterning on PMMA thin film and its subsequent application to nanoxerography. Adapted from [2].

as scanning probes [46, 44, 47, 48, 2, 8], focused ion beams [49], or liquid jets [50]. For example, AFM itself is a versatile instrument for charge writing, both positive and negative depends on the voltage applied [2]. As shown in Fig. 1.3, the AFM probe is polarized by the external voltage and the charges can be injected into the polymethylmethacrylate (PMMA) thin film. The desired charge pattern can be controlled by the scanning of the AFM probe with high spatial resolution. Right after the charge patterning, the surface potential distribution can be measured with KPFM. Various complicated surface charge patterns can be achieved, as shown by the potential images in Fig. 1.4. The electrostatically patterned samples are then incubated in the desired colloidal dispersion and then immersed in an adequate solvent for development. Final drying process leads to directly assembled nanoparticles guided by the charge pattern, as shown by the topography images in Fig. 1.4.

The direct writing method demonstrates high resolution, but the scanning rate is extremely slow and expensive infrastructures are usually required. In contrast to the serial direct writing, researchers developed an electrical contact printing method, in which a micropatterned electrode

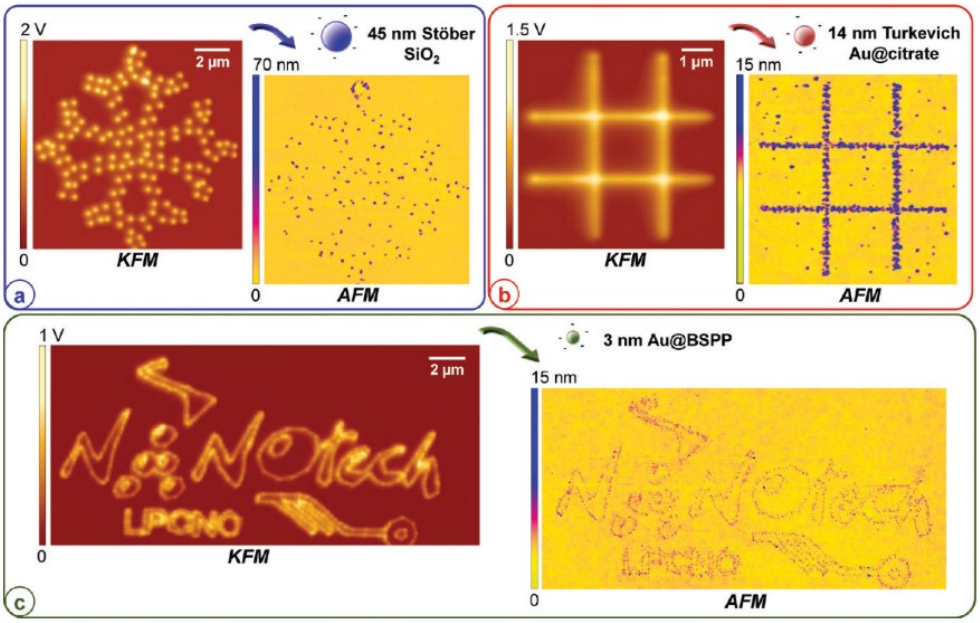

Figure 1.4 KPFM surface images and the topography images after the directed assemblies of various nanoparticles. Adapted from [2].

was placed in conformal contact with the target surface with an external voltage applied [51, 3, 52]. For example, Jacobs et al. developed the submicrometer patterning of charge based on the electric contact printing method [3]. The fabrication processes are shown in Fig. 1.5. The PDMS stamp with patterns was evaporated with Cr and Au to make the surface conductive. The metal-coated PDMS stamp was then placed in contact with the PMMA film on a n-doped silicon wafer. The contact between the PDMS electrode and the PMMA film is intimate thanks to the excellent flexibility of PDMS. Then an external voltage was applied in between the top PDMS electrode and the silicon substrate, leading to the electron transfer to the PMMA film. The corresponding charge pattern was determined by the initial pattern on the PDMS stamp.

This contact printing method enables the patterning of the material surface in a parallel process. In this method, however, the material surface to be patterned needs to be mounted on conductive surfaces, which serve as the opposite electrodes in the patterning process. To address this issue, the direct contact electrification [53] was developed, eliminating electrodes or any external biasing.

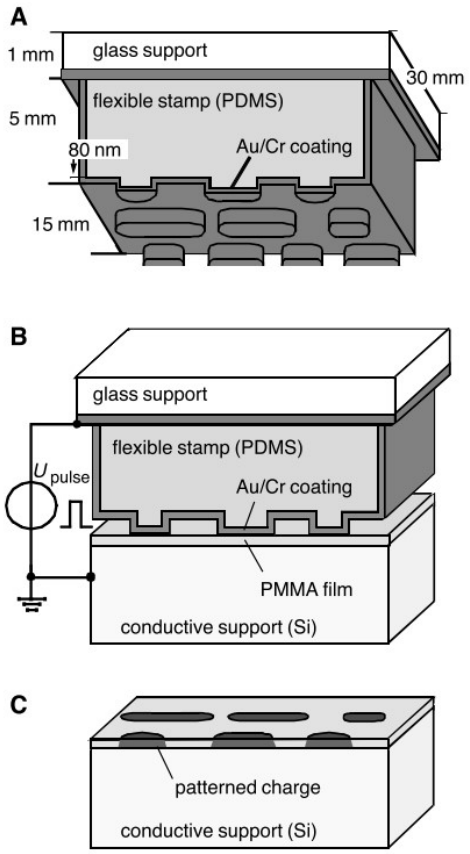

Figure 1.5 Principle of the electrical contact printing. Adapted from [3].

For example, the thermally [51] or chemically [52, 54] treated poly(dimethylsiloxane) (PDMS) stamps can be used to induce patterned surface charge through contact electrification without any electrodes or external biasing.

1.3 Dissertation Organization

This dissertation is consisted of six chapters, providing in Chapter 1 an overview of contact electrification and charge patterning techniques and corresponding applications. In Chapter 2, the working principles of the KPFM and EMF are described in detail. Their applications and limitations are also briefly discussed. Chapter 3 then presents our replica molding induced charge nanopatterning and the charge characterization results from the replica molding with different

materials combinations and varying interfacial morphologies. The electrostatic modeling is also described for the charge density estimation. Chapter 4 is dedicated to the finite element analysis of the replica molding process. A mechano-triboelectric model is established for the nanoscale contact electrification. The key factor is pointed out governing the final charge distribution pattern. Chapter 5 deals with an exemplary application of the generated nanopatterned surface charge on elastomer, that is, electrohydrodynamic naonlithography (EHDL). The numerical model of the EHDL process is established. In the final chapter, a brief summary and several future directions are discussed.

CHAPTER 2. SURFACE CHARGE CHARACTERIZATION TECHNIQUES

Before the introduction of our replica molding based charge nanopatterning technique, we will give an overview of the surface charge characterization techniques, especially those with nanoscale resolution based on scanning probe microscopy. In this chapter, we will start with an overview of the history of surface charge characterization techniques, especially the Kelvin method working in macroscopic scale. The second and third section present the working principles of scanning probe-based nanoscale surface charge characterization methods, Kelvin probe force microscopy (KPFM) and electrostatic force microscopy (EFM). Both will be extensively used throughout this dissertation. Then we will give an overview of the applications of KPFM and EFM in different fields. Finally, the scanning artifacts and limitations are briefly discussed.

2.1 Introduction

In 1898, Lord Kelvin originated a macroscopic method to measure surface electronic properties [4]. The metallic probe is vibrating above the sample surface to form a simple capacitor arrangement and the voltage applied to the probe is adjusted so that no current is induced by the vibration, as shown in Fig. 2.1. The induced current is written as

$$I_{\mathrm{dc}} = \frac{dC}{dt}\left(V_{\mathrm{bias}} - V_{\mathrm{CPD}}\right) \tag{2.1}$$

where C is the capacitance between probe and sample, V_{bias} is the external voltage applied and V_{CPD} is the contact potential difference between the probe and sample surface. Here the presence of surface charge is not considered and will be discussed in detail later. Thus the voltage applied to the probe when the induced current is zero measures the contact potential difference between the probe and the sample surface. When using probe made of inert material (gold, platinum, iridium) with well defined work function, the sample surface potential can be determined. The

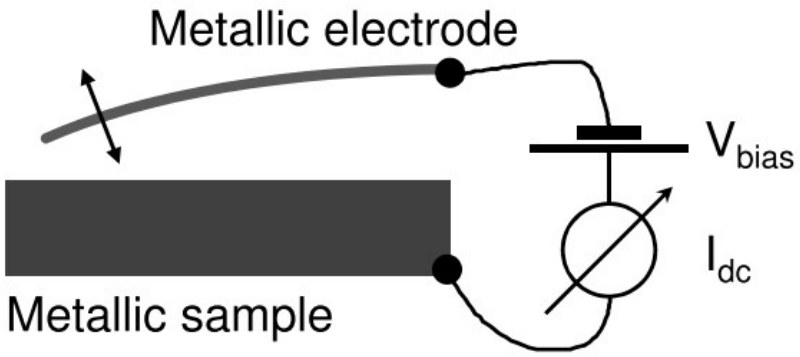

Figure 2.1 Scheme of the Kelvin method working in the macroscopic scale. Adapted from [4]

spatial resolution depends on the probe size and scanning step size and is usually around 0.3 mm [55].

When extending this principle to the micro- or nano- scale, however, the sensitivity is very poor since the induced current is insufficient from capacitor with small plate size, especially with a probe size of tens of nanometer. Instead, the electrostatic force between the probe and sample surface was utilized. To achieve a lateral resolution in the nanometer range, the Kelvin method was combined with the atomic force microscopy (AFM), which was invented in 1986 [56] to solve the limitation that only conducting surfaces can be used in scanning tunneling microscopy (STM) [57]. Before describing the microscopic version of the Kelvin method, we will briefly introduce the working principle of AFM, especially the tapping mode.

In the early stage, the AFM was working in the contact mode and the sample surface could be damaged or deformed due to the lateral forces between the scanning probe and sample surface (Fig. 2.2), especially for biological and polymeric materials. The non-contact mode AFM was later developed to minimize the interaction force between the scanning probe and the sample surface by maintaining the contact only for a short time, the so-called tapping mode. In the tapping mode, the cantilever oscillates at its resonance frequency and the probe is in touch with the sample surface

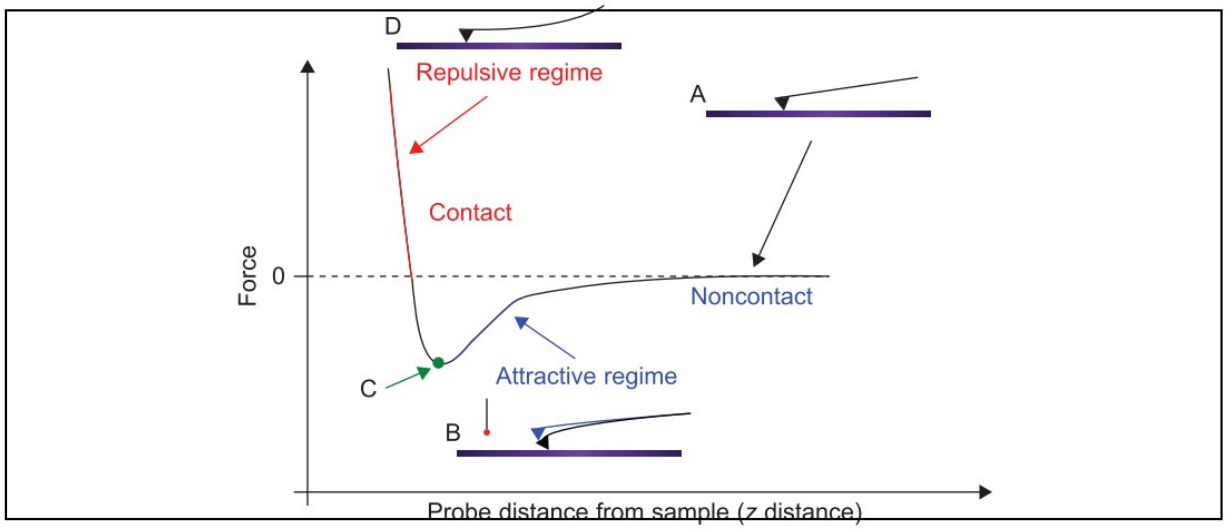

Figure 2.2 Interatomic force versus distance curve. Adapted from [5]

for a short period of time at each cycle. In Fig. 2.2, the cantilever is oscillating intermittently in the attractive regime and repulsive regime. During the scanning, the oscillating amplitude at the operating frequency is maintained at a constant level, realized with the amplitude setpoint, so that the relative position between the probe and sample surface is kept the sample. Thus the trace of the probe reflects the topography variation of the sample surface.

2.2 Kelvin Probe Force Microscopy

Kelvin probe force microscopy is a representative combining the non-contact atomic force microscopy and the Kelvin method. It was first reported by Nonnenmacher et al. [58] and Weaver et al. [59] in 1991. The main enabling factor of KPFM is the sensitive cantilever beam that can measure the electrostatic force by employing an optical readout on the back side of the cantilever. Thus the local contact potential difference or surface charge distribution can be accessed. It's typically implemented in a two-pass scheme, as shown in Fig. 2.3. In the first pass, the surface topography is measured in the tapping mode by maintaining a contact distance between the probe and the sample surface. In the second pass, the probe is lifted up by tens of nanometer based on the

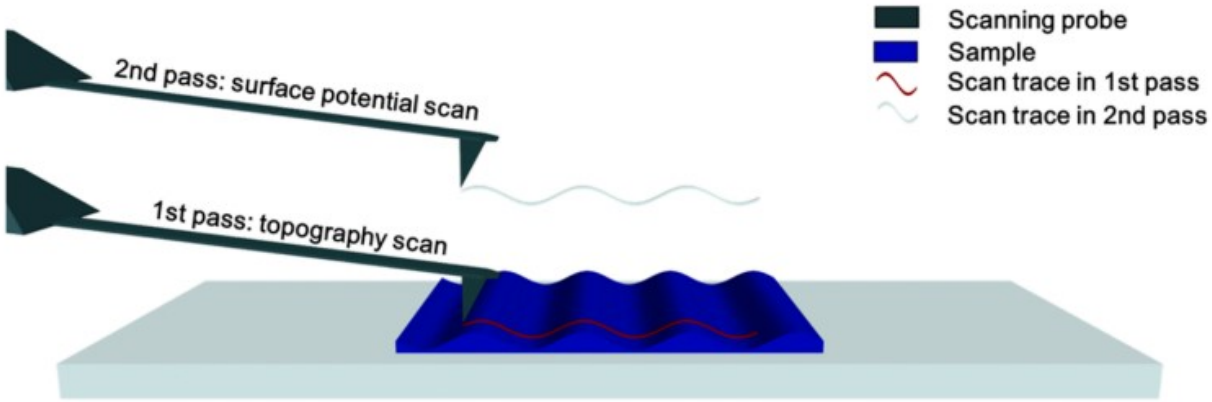

Figure 2.3 Schematics of the working principle of the KPFM implemented in a two-pass scheme. Adapted from [6]

stored topography information to measure the long-range electrostatic force. This can eliminate the inaccuracy caused by the variation of the distance between the probe and sample surface.

In a typical KPFM setup, an ac-voltage $V_{\mathrm{ac}} \sin(\omega_{\mathrm{ac}} t)$ is applied to oscillate the cantilever and a dc-voltage V_{dc} is applied to compensate the electrostatic force in the second pass. With a parallel-capacitor model, the electrostatic force can be expressed as

$$F_{\mathrm{el}} = -\frac{1}{2}\frac{\partial C}{\partial z}\left[V_{\mathrm{dc}} - V_{\mathrm{CPD}} + V_{\mathrm{ac}} \sin\left(\omega_{\mathrm{ac}} t\right)\right]^2 \tag{2.2}$$

in which V_{CPD} is the contact potential difference between probe and sample.

The electrostatic force can be decomposed to three terms, dc component, single-frequency component, and double-frequency component.

$$F_{\mathrm{dc}} = -\frac{\partial C}{\partial z}\left[\frac{1}{2}\left(V_{\mathrm{dc}} - V_{\mathrm{CPD}}\right)^2 + \frac{V_{\mathrm{ac}}^2}{4}\right] \tag{2.3}$$

$$F_{\omega_{\mathrm{ac}}} = -\frac{\partial C}{\partial z}\left(V_{\mathrm{dc}} - V_{\mathrm{CPD}}\right) V_{\mathrm{ac}} \sin\left(\omega_{\mathrm{ac}} t\right) \tag{2.4}$$

$$F_{2\omega_{\mathrm{ac}}} = \frac{\partial C}{\partial z}\frac{V_{\mathrm{ac}}^2}{4} \cos\left(2\omega_{\mathrm{ac}} t\right) \tag{2.5}$$

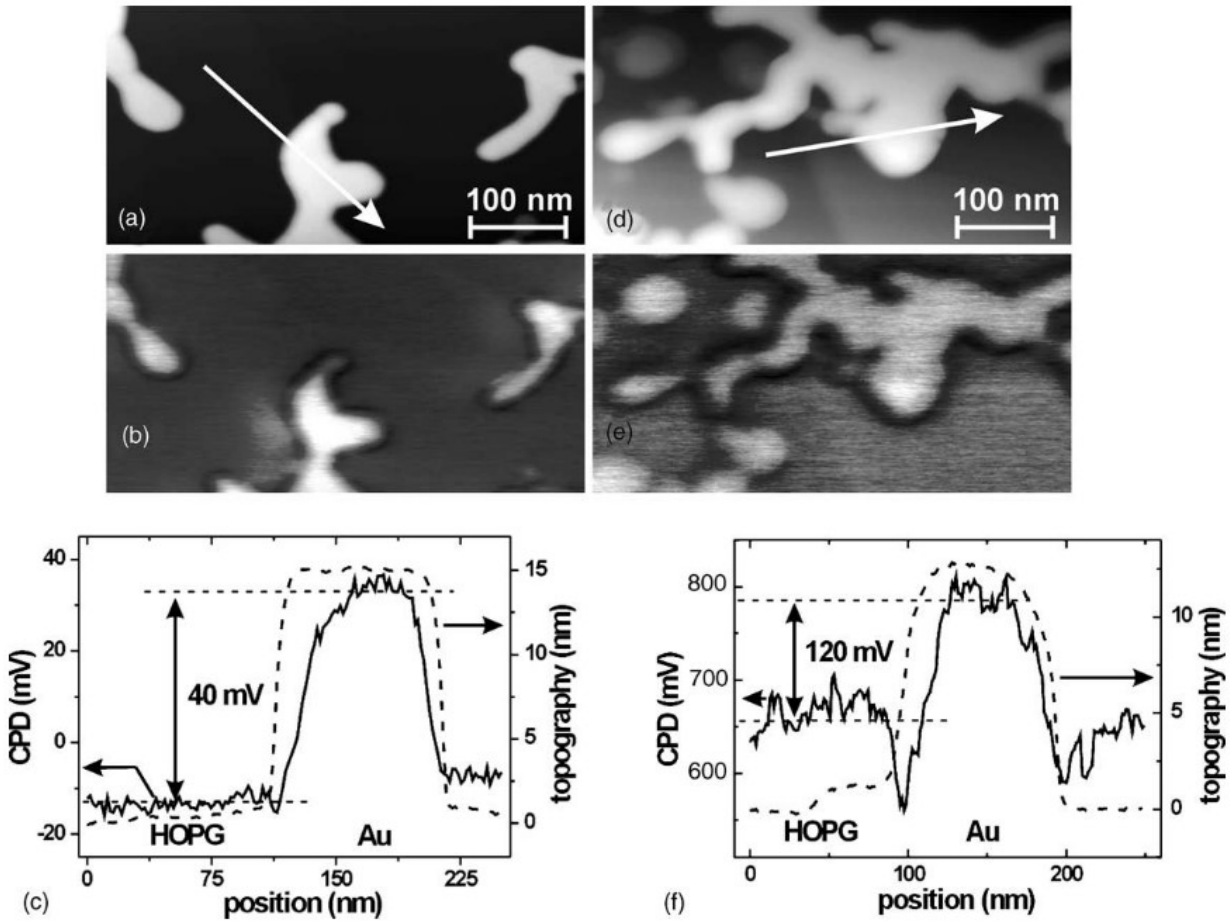

Figure 2.4 AM- and FM-mode measurements on a HOPG sample with Au islands. Adapted from [7]

The applied dc-voltage is adjusted to minimize the single-frequency component, leading to $V_{\mathrm{CPD}} = V_{\mathrm{dc}}$. This technique results in similar surface potential imaging as that in the conventional Kelvin method, but with much higher spatial resolution and sensitivity in the surface potential.

There are mainly two different working modes in KPFM depending on the feedback variable utilized during the scanning, amplitude modulation (AM) and frequency modulation (FM). In AM mode, the applied dc-voltage is controlled by minimizing the amplitude of the induced oscillation at the ac-frequency to zero, as described above. While in the FM mode, the variation in the frequency shift at the ac-frequency is minimized. In other words, the scanning probe senses the force gradient

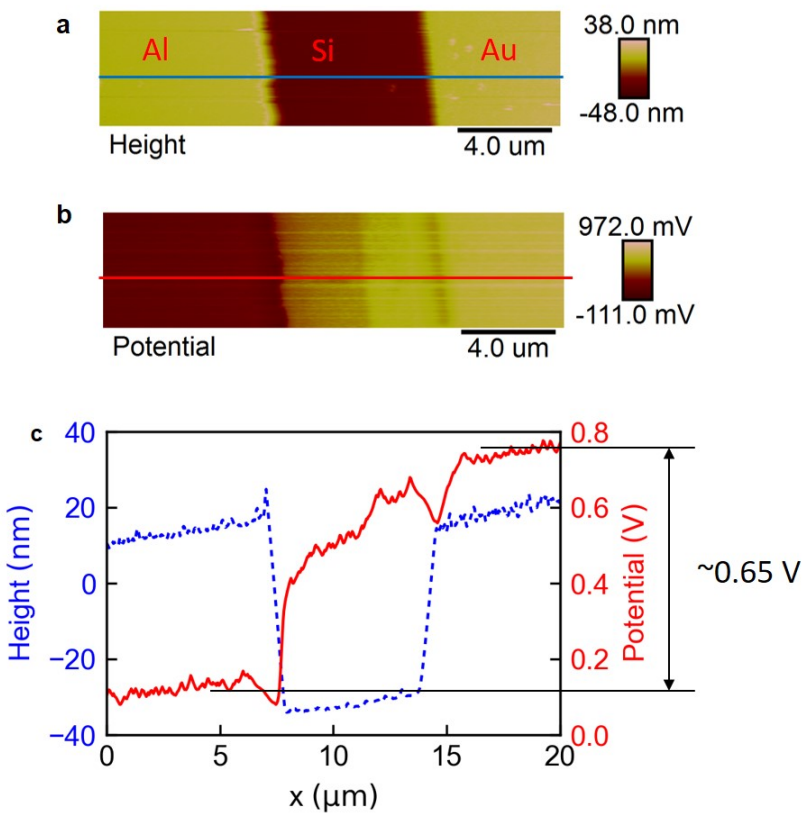

Figure 2.5 The KPFM measurement on the testing sample consisted of gold and aluminum patterns on a silicon wafer. The thickness of gold and aluminum is around the same, while the contact potential difference shows different values, reflecting the difference in work function of different materials.

generated from the contact potential difference

$$\Delta f_0\left(\omega_{\mathrm{ac}}\right) \propto \frac{\partial F_{\omega_{\mathrm{ac}}}}{\partial z} = \frac{\partial^2 C}{\partial z^2}\left(V_{\mathrm{dc}} - V_{\mathrm{CPD}}\right) V_{\mathrm{ac}} \sin\left(\omega_{\mathrm{ac}} t\right) \tag{2.6}$$

As described by the above equation, the AM mode is sensitive to the electrostatic force, while the FM mode is sensitive to the electrostatic force gradient. They are different in terms of the spatial resolution and resolution in the contact potential difference. One example is the study on dendritic gold islands on highly oriented pyrolytic graphite (HOPG) with both operation modes [7]. The results are shown in Fig. 2.4. The contact potential difference between gold and graphite is around 40 meV and 120 meV in the AM mode and FM mode, respectively. This large difference

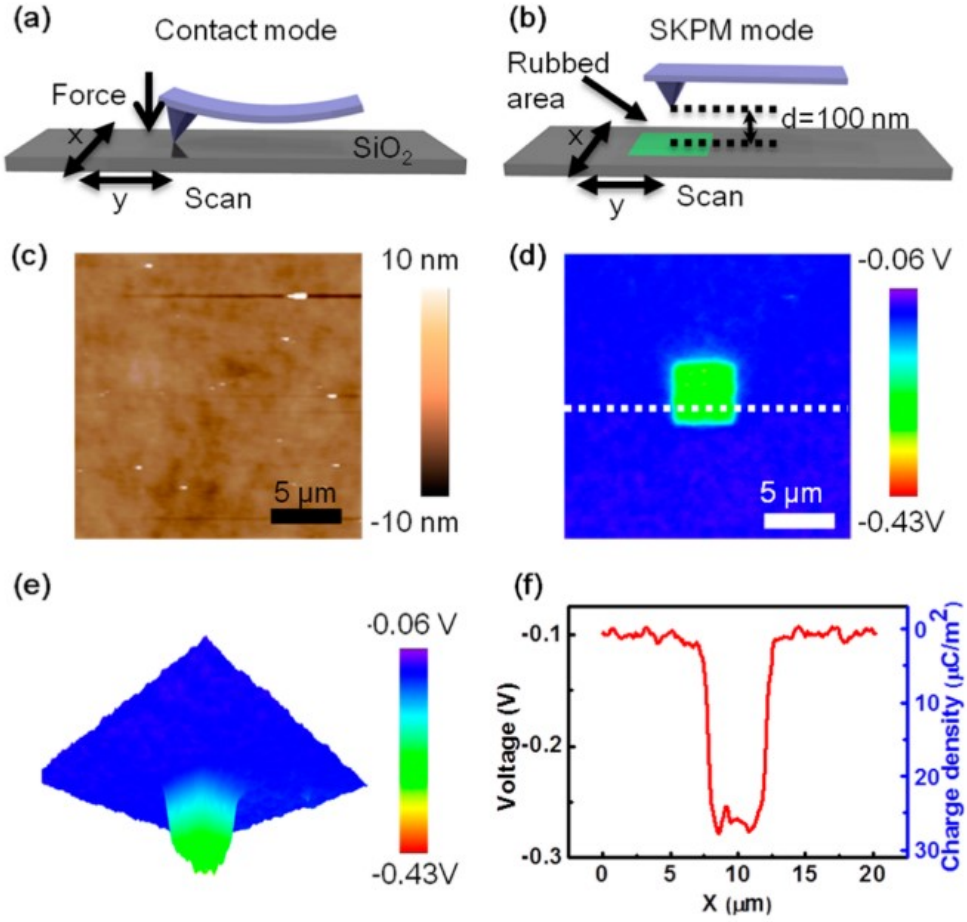

Figure 2.6 Schematics and results of the KPFM used to characterize the surface charge distribution induced by the contact mode AFM. Adapted from [8].

can be explained by the fact that the AM mode is sensitive to the long range electrostatic force and thus can sense a larger area. The measured contact potential difference is actually an average over a large area. In the FM mode, however, the electrostatic force gradient is relatively short-ranged and the average is over a relatively smaller area, leading to larger contrast in the measured contact potential difference. Similarly, the spatial resolution is also better in FM mode, as shown in Fig. 2.4.

After its invention, KPFM has been widely used in solar cell materials [60], adatoms and admolecules [61, 62], low-dimensional systems [63, 64, 65, 66], local work function [67], biological systems [68, 69, 70]. A basic example is the work function difference of different material like

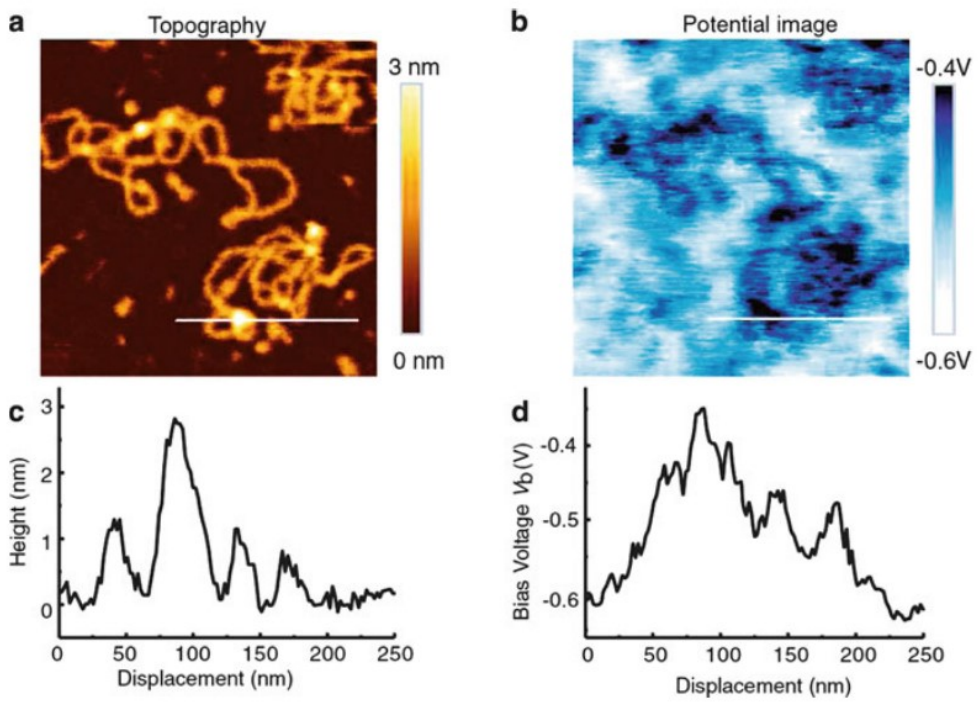

Figure 2.7 KPFM results of DNA and transcription complexes of DNA. Adapted from [9].

metals or semiconductors. For example, a commonly used testing sample is the gold and aluminum patterns on a silicon wafer. The surface topography and surface potential maps are shown in Fig. 2.5a and b, respectively. The cross sectional scans along the blue line in a and red line in b are superimposed in c for facile comparison. It's clear that the thickness of the aluminum and gold films is around the same, $\sim$ 50 nm. The surface potential scanning, however, shows a difference around 0.65 V between aluminum and gold. Considering the same AFM probe used in the scanning, this difference in surface potential originates from the work function difference between aluminum and gold. The work function [71] of aluminum and gold is around 4.06-4.26 eV and 5.10-5.47 eV. The difference is in good agreement with the measured difference in surface potential.

The KPFM can be also used for the surface charge imaging on insulators. For example, the contact mode AFM was used to induce the contact electrification at nanoscale and the following KPFM mode scanning characterized the surface charge distribution and subsequent diffusion [8]. As shown in Fig. 2.6, the AFM was first operated in contact mode to induce friction patterns on

the SiO_2 film. The surface topography and surface potential were then subsequently measured *in situ* with KPFM. The surface topography shows negligible variation while the surface potential shows a clear contrast between the rubbed and intact areas. Since the work function difference is the same across the whole area, the contrast in the surface potential is attributed to the induced surface charge. The surface charge density can be estimated from the surface potential difference between the rubbed and intact area ΔV with a parallel capacitor model

$$\sigma = \frac{\Delta V \varepsilon_0 \varepsilon_{SiO_2}}{t_{SiO_2}} \tag{2.7}$$

where ε_0 is the vacuum dielectric constant, t_{SiO_2} and ε_{SiO_2} are the thickness and relative dielectric constant of SiO_2, respectively.

In biological systems, KPFM can also be applied to measure the surface potentials and electrostatic interaction, including voltage-gated ion channels, protein folding and assembly, and electroactive cells and electrotransduction. One example is the stretched single DNA molecules [9] shown in Fig. 2.7. The dark area of the surface potential image shows low electric potential, corresponding to the DNA and the polymerase transcription complex.

2.3 Electrostatic Force Microscopy

Instead of compensating the electrostatic force by applying a dc-voltage in KPFM, it's also possible to measure the magnitude of the force directly, that is, the EFM. It has been widely used for charge characterization on insulators such as epoxy resin[72], nanocomposite[13], and adatoms[10]. By tracking the electrostatic force generated by the surface charge, EFM can directly measure the charge's polarity and density even on highly insulating substrates[73, 11], complementing the results of KPFM.

In our setup, the sample substrate was grounded and we measured the resonance frequency shift Δf_0 of the cantilever probe as a function of the dc-voltage V_{dc} applied to the probe. The frequency shift is proportional to the gradient of the force, as given by [72, 73, 11]

$$\frac{\Delta f_0}{f_0} \approx -\frac{1}{2k_c}\frac{dF_{dc}}{dz} = -\frac{1}{2k_c}\frac{d}{dz}\left(\frac{1}{2}C'V_{dc}^2 + \frac{q_s q_t}{4\pi\epsilon_0 z^2}\right) \tag{2.8}$$

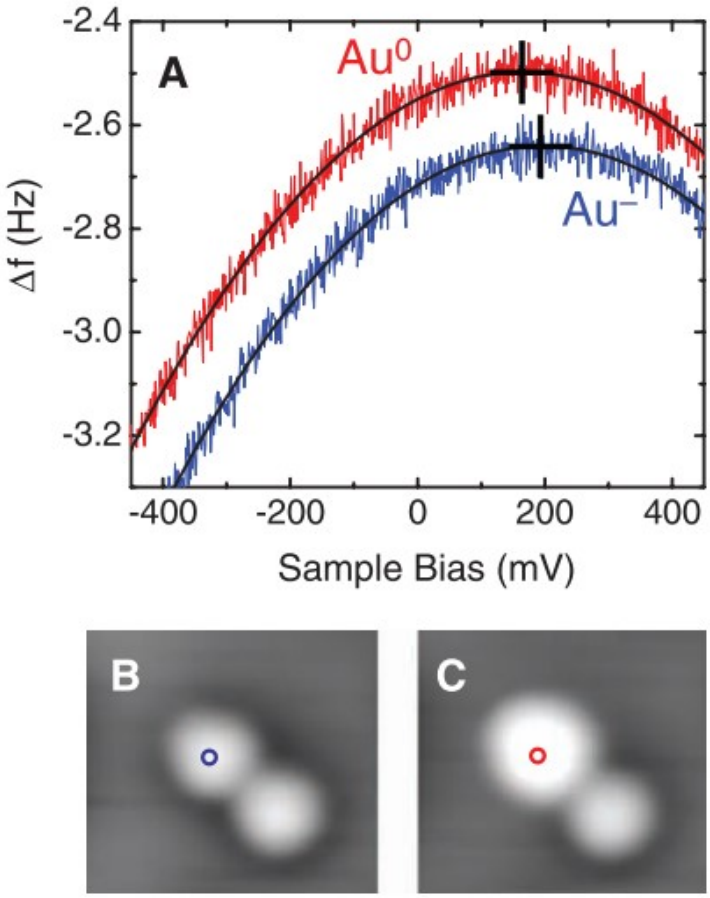

Figure 2.8 (a) EFM results of the measurement above Au^- and Au^0. (b) and (c) are the STM images before and after the EFM measurements, confirming the charging-switching event and the lateral position is maintained. Adapted from [10].

where f_0 is the resonance frequency of the probe, k_c is the cantilever spring constant, z is the vertical distance between the sample surface charge q_s and the image charge $q_t = -q_s + C \cdot V_{dc}$ on the probe. F_{dc} is the force exerted on the probe, consisting of the capacitive contribution and the Columbic attraction, where C is the probe to substrate capacitance and C' the first derivative with respect to z.

Carrying out the differentiation in Eq. 2.8 reveals that the resonance frequency shift Δf_0 is quadratically related to V_{dc} as

$$\Delta f_0 = -\frac{f_0}{2k_c}\left(\frac{C''}{2}\cdot V_{dc}^2 - \frac{q_s}{4\pi\varepsilon_0}\left(\frac{2C}{z^3} - \frac{C'}{z^2}\right)\cdot V_{dc} + \frac{q_s^2}{2\pi\varepsilon_0 z^3}\right) \tag{2.9}$$

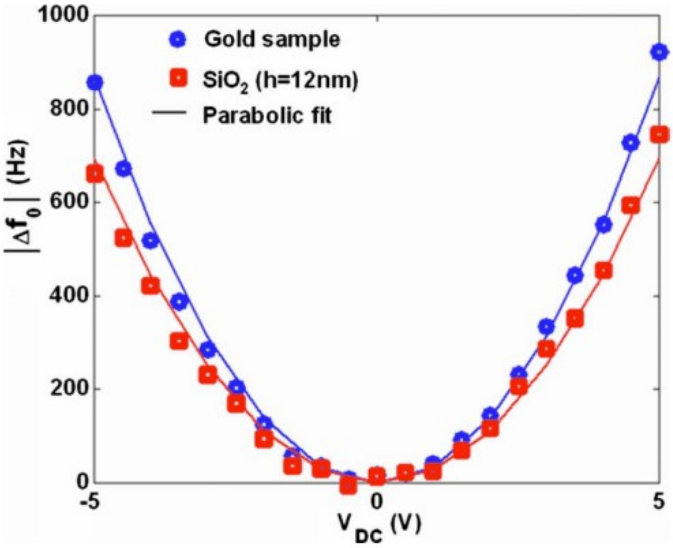

Figure 2.9 The EFM results of the 12 nm thick SiO_2 film on gold surface. Adapted from [11].

It is straightforward to show that the frequency shift Δf_0 maximizes at

$$V_{\mathrm{dc}}^{*} = \frac{q_s}{4\pi\varepsilon_0}\frac{1}{C''}\left(\frac{2C}{z^3} - \frac{C'}{z^2}\right) \tag{2.10}$$

With $\frac{1}{C''}(\frac{2C}{z^3} - \frac{C'}{z^2})$ always positive, the polarity of the surface charge can be determined from the sign of V_{dc}^{*}. In addition, the surface charge q_{s} itself can be determined from the y-intercept as

$$|q_{\mathrm{s}}| = \sqrt{\frac{4\pi\varepsilon_0 k_{\mathrm{c}} h_{\mathrm{v}}^3 \left|\Delta f_0 \left(V_{\mathrm{dc}} = 0\right)\right|}{f_0}} \tag{2.11}$$

Thus, we are able to determine the charge polarity and magnitude with EFM.

The typical results from EFM measurement is the quadratic dependence of the frequency shift as a function of the applied dc voltage, as evidenced by equation 2.9. In Fig. 2.8, the gold atom sitting on top of an ultrathin NaCl layer was measured with EFM first. Then the charge state was switched by applying a bias voltage pulse of about -1 V for a few seconds. After switching, the EFM measurement was done again. The parabolic fitting shows that the contact potential difference of Au^{-} has shifted by around 30 meV.

The EFM has also been used to determine the nanoscale dielectric constant of thin insulating layers [11]. The 12 nm thick SiO_2 film was deposited on the gold surface and the measured with

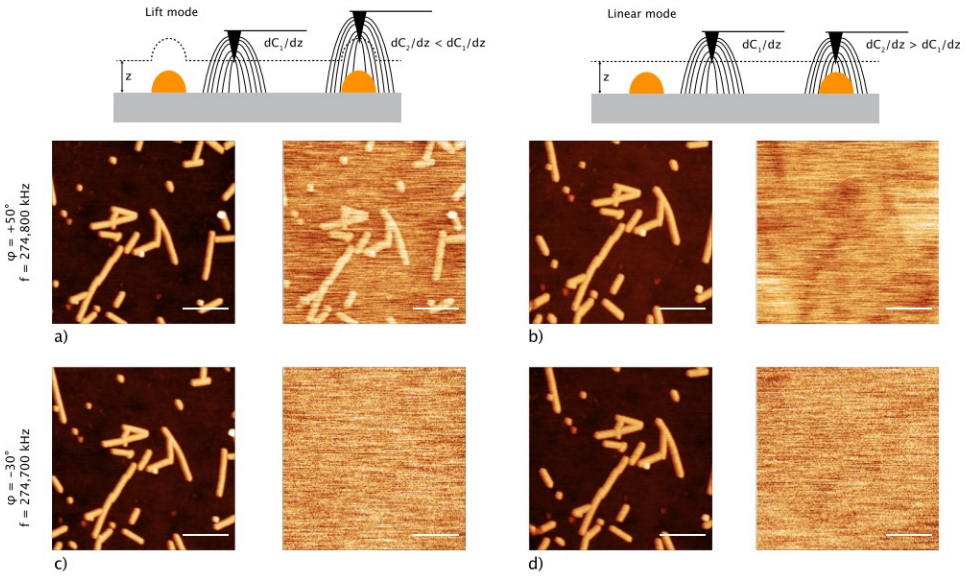

Figure 2.10 Topography and KPFM images of tobacco mosaic viruses deposited on silicon dioxide. Scale bars are 500 nm. Colour scales are 25nm (topography images) and 3mV (KPFM images). Top: images containing ac cross-talk effects Bottom: images free of ac cross-talk effects. Adapted from [12].

EFM. The quadratic fitting of the frequency shift dependence on the applied voltage gives the estimation of the dielectric constant. This also enables label-free identification of materials with different dielectric constants [74].

2.4 Artifacts and Limitations

From the principle of KPFM, the single-frequency component of the electrostatic force $F_{\omega_{\mathrm{ac}}}$ should be nullified. The contact potential difference can be determined independently from measurement parameters. However, this condition is usually difficult to reach in real experiments and the measured contact potential difference V_{CPD} is affected by the measurement environments, tip geometry, instruments effects, and chosen experimental parameters. A detailed overview of all the artifact and limitations is out of the scope of this thesis and can be found in [75, 76, 77]. In this section, we will mainly discuss the cross-talk effect from the topography and the limitations from the experimental point of view.

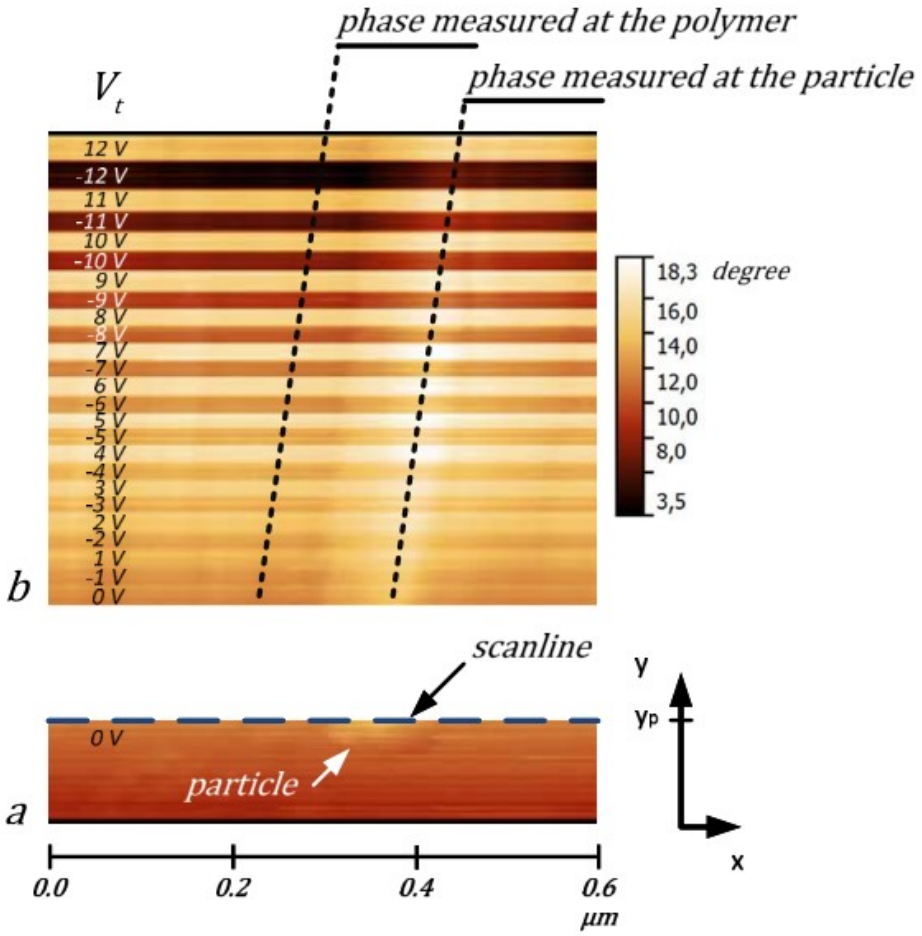

Figure 2.11 EFM image measured at a filler particle with varying tip-sample bias. Adapted from [13].

As shown in Fig. 2.10, the most important effect of the cross-talks is the artificial footprint of the sample topography onto the KPFM images [12]. In Fig. 2.10, the tobacco mosaic viruses (TMVs) were transferred to the silicon dioxide substrate. It's known that no charge transfer occurs in this process. The TMVs were then investigated using KPFM with or without cross-talks by setting different drive phase. From the comparison of the topography image and potential image, it's obvious that the cross-talks causes the footprint of the topography image onto the potential measurement, leading to surface potential variations that doesn't really exist.

Another limitation of EFM is that the data collection during the scanning needs to be done for multiple applied dc-voltage, as shown in Fig. 2.9. Figure 2.11 also shows the scanning with different dc-voltage applied to the probe. This means the scanning time taken in the measurement is several time longer than that in KPFM since multiple frames of the map need to be collected and the parabolic fitting is then used to determine the measurement variables.

CHAPTER 3. REPLICA MOLDING-BASED NANOPATTERNING OF TRIBOCHARGE

In this chapter, we will start with the fabrication process of our replica molding-based charge patterning technique. The following two sections deal with how the nanopatterned tribocharge is affected by the different material combinations and interfacial morphology. Later part of this chapter presents the electrostatic molding to estimate the surface charge density in the special ring-type charge distribution.

3.1 Replica Molding-based Nanopatterning of Tribocharge on Elastomer

Tribocharging of elastomer surface is attracting substantial interest, with the resulting tribocharges already playing crucial roles in energy harvesting, mass spectrometry, and electronics. The tribocharge's origin, although still under study, is often attributed to the transfer of electrons or ions between material surfaces during their electrical or frictional contact. Of recent interest is the tribocharging of poly(dimethylsiloxane) (PDMS) surface after replica molding which turns out to be strong enough to influence microfluidic channel electrophoresis. It is rather ironic that such replica molding-induced tribocharging phenomenon has been studied only on untextured elastomer surfaces, such as microfluidic channel walls, given that replica molding is a very effective method for their nanotexturing. Questions regarding how such nanotexturing impacts the generation and distribution of the tribocharge are not answered yet.

Here, we carry out a multi-physical study to answer the questions and also to establish a useful application for the intriguing phenomenon. It also turns out to be a straightforward charge nanopatterning method. As our model nanostructure, we used arrayed PDMS nanocups replicated from a polycarbonate (PC) nanocone array (Fig. 3.1).

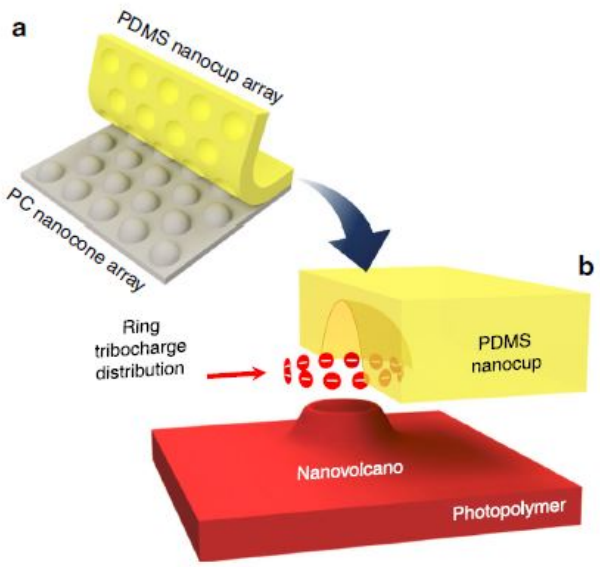

Figure 3.1 Replica molding-based tribocharging and its use in EHDL. **a** After being replica molded from a nanotextured polycarbonate (PC) mold, the elastomer replica's surface acquires tribocharges distributed in close correlation with the nanotexture. **b** The resulting electric field can subsequently shape the photopolymer at nanoscale through EHDL. In this work, the PDMS nanocup, replicated from a PC nanocone, acquires a nanoring-shaped tribocharge which shapes the photopolymer into a nanovolcano

To fabricate the tribocharged PDMS nanocup array, we first prepared a PC mold with a 750 nm-pitch triangular array of nanocones (500 nm in base diameter, 150 nm in height, about 1×1 cm^2, Microcontinuum Inc.) and then poured liquid phase PDMS (Sylgard 184, Dow Corning) mixed with the curing agent at 10:1 wt. ratio. Upon its complete solidification, we peeled it off from the mold, obtaining a matching array of nanocups. The surface topography, examined with scanning electron microscopy and atomic force microscopy (AFM) in the tapping mode, are shown in Fig. 3.2 and Fig. 3.3a, respectively. The average depth d was 153 ± 13 (s.d.) nm. To elucidate the polarity and the distribution pattern of the tribocharges on the replica molded PDMS surface, the surface potential was also measured through KPFM and plotted in Fig. 3.3b.

From the comparison of the scans in Fig.3.3a, b, it is evident that the positions of the negative potential wells closely match those of the nanocups' apertures. The surface topography and po-

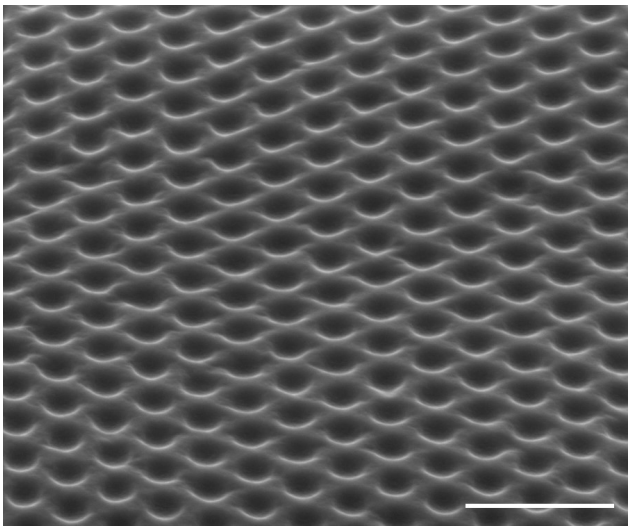

Figure 3.2 Morphology of PDMS nanocups This scanning electron micrograph of the PDMS nanocups, taken with the sample stage tilted by 55 degrees, clearly shows the regularly arrayed apertures of the nanocups and the flat interstitial area between them. Scale bar: 2 μm.

tential profiles shown in Fig. 3.3c, superimposed for facile comparison, further confirm their close correlation. Since the work function difference between the PDMS surface and the AFM probe is almost the same across the scanning area, the wells in the surface potential are induced mainly by the tribocharges [8]. It also indicates that the PDMS surface was negatively charged, which agrees well with the negative tribocharging of PDMS by PC reported by Baytekin et al. [1]. Interestingly, the surface potential exhibits peaks near the center of the nanocups, which yields valuable information on the charge distribution within the nanocups.

3.2 Effect of Materials Combination

To investigate the effect of different material combinations on the generated nanopatterned tribocharge, we adopted poly(ethyleneterephthalate) (PET) plates (Microcontinuum Inc.) nanotextured with triangular nanocone arrays. The pitch, diameter, and height are identical to the PC master used in the previous chapter. The charge-affinity of polycarbonate is lower than that of PET [78]. The replicated PDMS nanocups were examined with KPFM in a similar manner.

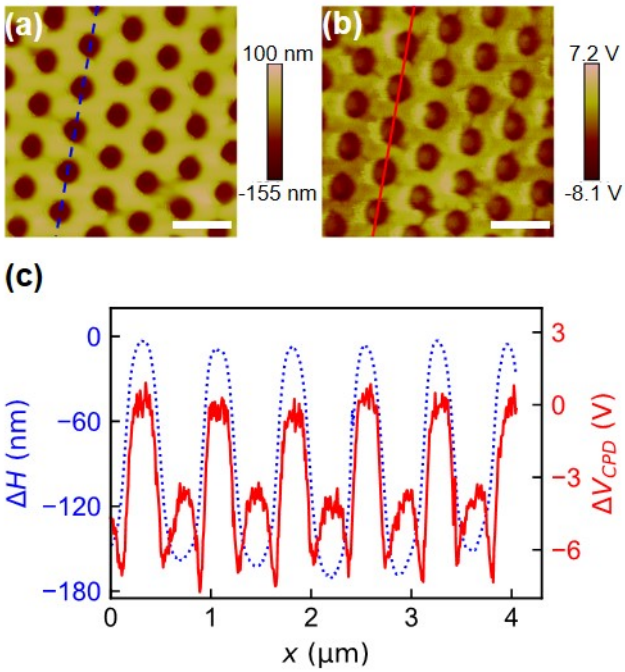

Figure 3.3 **KPFM-based imaging and analysis of tribocharge distribution.** **a** AFM image of the PDMS nanocup array's surface topography. **b** KPFM image of the surface potential V_{CPD} at the same spot. (Scale bars: 1 μm) **c** Superimposed cross-sectional profiles of the surface topography and potential along the scan lines in **a**, **b**. The pattern overlap clearly indicates that the inner cavity of the nanocup is negatively charged.

Figure 3.4a, b show the topography and surface potential, respectively. Their cross-sectional profiles, obtained along the dotted and solid lines in Fig. 3.4a,b, respectively, are superimposed in Fig. 3.4c for facile correlation. Aside from a slight azimuthal asymmetry, the potential pattern takes the form of a ring and is located primarily around the nanocup's rim. Compared with the case of PC/PDMS combination, the only significant difference is the vertical flipping of the surface potential profile. Fig. 3.4c shows that the ring-shaped potential we just obtained from the PET mold takes a "dip-in-the-peak" profile which is a signature trait of a positive ring-charge [3]. In the previous case based on PC master molds, however, we observed a "peak-in-the-well" potential profile. It is inverse to the "dip-in-the-peak" profile and also a signature trait of the negative

ring-charge. This suggested reversal of polarity indicates that the charge affinity of PDMS may lie between those of PC (-5 nC/J) and PET (-40 nC/J) [78].

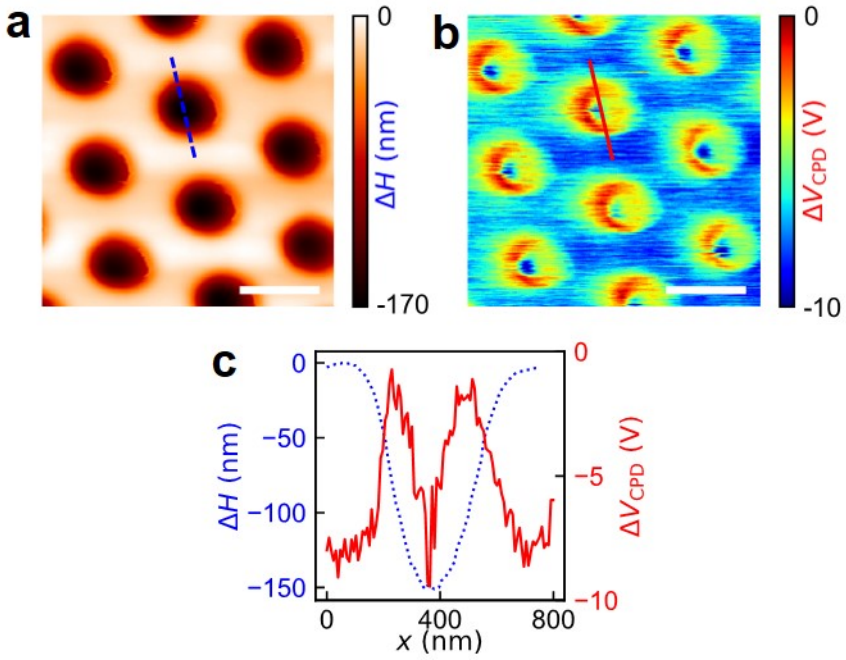

Figure 3.4 KPFM-based imaging and analysis of tribocharge distribution of the PDMS nanocups replicated from PET. **a** AFM image of the PDMS nanocup array's surface topography. **b** KPFM image of the surface potential V_{CPD} at the same spot. (Scale bars: 500 nm) **c** Superimposed cross-sectional profiles of the surface topography and potential along the scan lines in **a**, **b**.

3.3 Effect of Surface Topography

With our basic conjecture on the aspect ratio's role in the nanoscale CE reaffirmed, we proceeded to investigate how the changes in the aspect ratio affect the nanoscale CE. we adopted PET plates with three different types of triangular nanocone arrays. No surface modification, physical or chemical, was performed to the master mold. Figure 3.5c shows the basic geometry of the PDMS nanocups demolded from the PET nanocones. The radius a and center-to-center spacing p of the

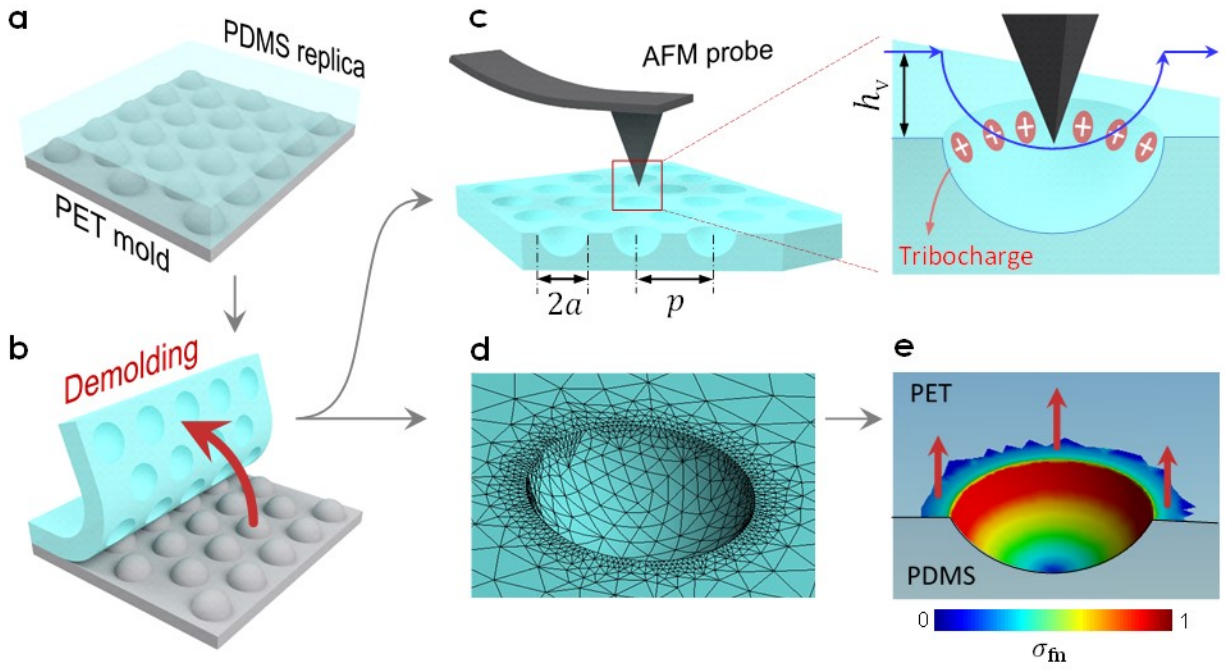

Figure 3.5 (a) A nanocone-textured PET mold is replicated with PDMS. (b) Demolding of the PDMS replica tribocharges the PDMS surface. (c) The PDMS surface is characterized by AFM, KPFM, and EFM. The blue curve indicates the tip's scanning path during KPFM and EFM. a, p, and h_v represent the nanocup's aperture radius, center-to-center spacing, and the tip-surface separation which, in our setup, are 250, 750, and 100 nm, respectively. The nanocup's depth h was varied. (d) The setup for finite element analysis of the demolding action. (e) The computed distribution of the normalized frictional stress σ_{fn} on a PDMS nanocup ($h = 153$ nm). The red arrows indicate the direction of replica/mold separation.

nanocone were fixed at 250 and 750 nm, respectively. The nanocone's height (hence the nanocup's depth) h was varied to be 154.3 ± 7.8 nm (sample A), 93.5 ± 8.5 nm (sample B), and 50.2 ± 1.1 nm (sample C). The corresponding aspect ratios (AR $\equiv h/a$) were 0.62, 0.37, and, 0.20, respectively. Upon demolding, we probed the nanocups by atomic force microscopy (AFM) and KPFM (Fig. 3.5c) to study the nanotexture's impact on the friction and charge distribution

We used samples B and C which exhibit increasingly lower aspect ratios of 0.37 and 0.20, respectively. The second and third columns of Fig. 3.6 show the results. Comparison of the KPFM results, facilitated by their juxtaposition, reveals that the charge distribution pattern in each

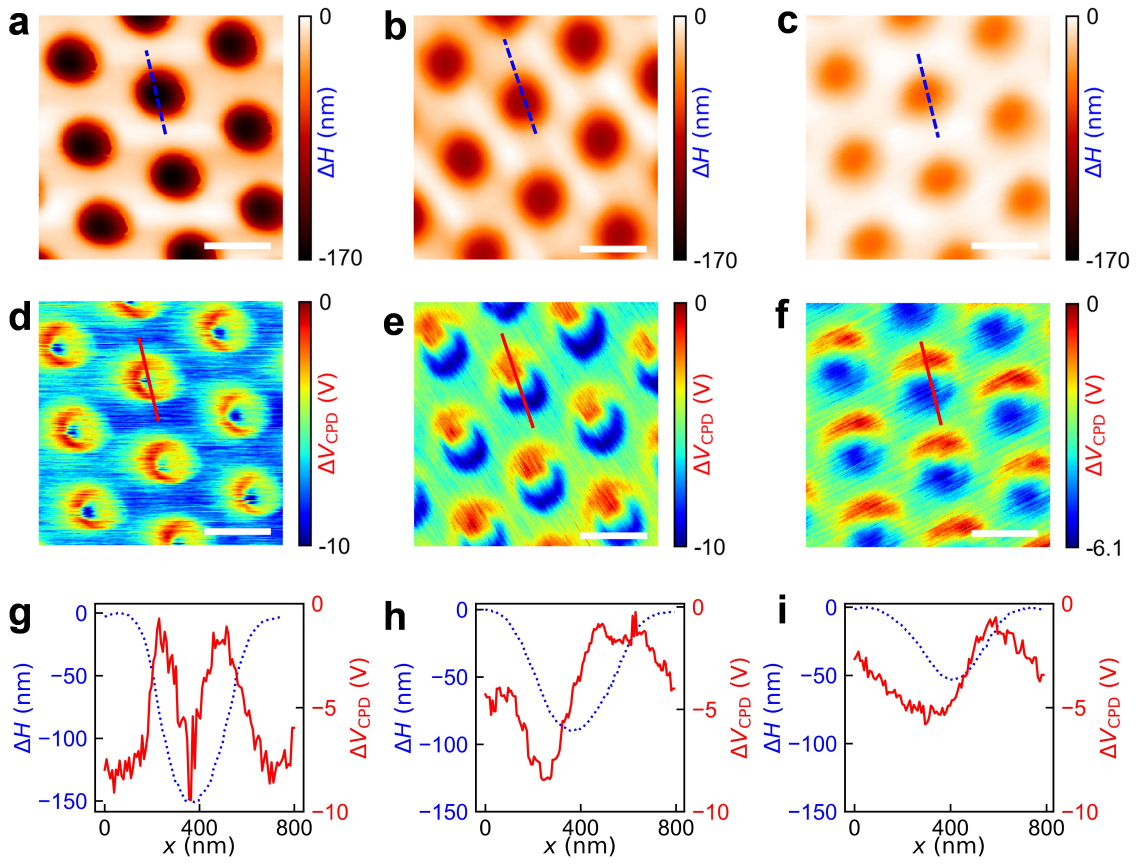

Figure 3.6 AFM surface topography (a-c) and the corresponding surface potential maps (d-f) of the samples A (AR = 0.62), B (AR = 0.37), and C (AR = 0.20), respectively. (g-i) The topographic and potential scans obtained along the blue dashed lines in (a-c) and the solid red lines in (d-f), respectively, are superimposed for facile correlation. (Scale bars: 500 nm.)

nanocup changes gradually yet significantly from the original ring-shape (AR = 0.62) to a partial eclipse (AR = 0.37) and a dumbbell (AR = 0.20) as the aspect ratio decreases. The nanotexture indeed controls the friction pattern through its shape. Note that the potential variation across the PDMS nanocups becomes lower as the aspect ratio decreases due most probably to the weaker frictional stress during the demolding action.

Note that the red-to-blue transitions in Fig. 3.6d-f indicate the decrease in the surface potential level generated by the tribocharges but not necessarily reversals in their polarity. The highly insulating nature of PDMS and the substantial thickness of the PDMS nanocup array (> 1 mm)

made it impossible to directly determine the surface potential or the tribocharge's polarity in the absolute sense. This issue will be addressed in the next chapter with the help of EFM.

3.4 Electrostatic Modeling

To extract more information from the KPFM results in Fig. 3.3, we performed iterative electrostatic modeling which reconstructs the charge distribution by repeatedly adjusting the model charge distribution until the resulting electric potential exhibits a good agreement with the experimental measurement. Among the salient features of the KPFM result in Fig. 3.3b, c, of special concern was the peak inside the potential well.

To compute the electric potential arising from the electric charges distributed on the nanocup's inner cavity surface, we first decomposed the inner cavity surface into a stack of thin annular strips with varying radii. Then we multiplied the preset surface charge density ρ_s to the surface area of each annular strip to determine the corresponding total charge. We then modeled each annular strip as a ring charge distribution. The electric potential V arising from a ring charge distribution with radius a is given in closed form as [79]

$$V = \frac{Q}{2\pi^2\epsilon_0} \cdot \frac{K(\sqrt{\frac{4a\rho}{a^2+\rho^2+h^2+2a\rho}})}{\sqrt{a^2+\rho^2+h^2+2a\rho}} \tag{3.1}$$

where Q, ρ, h, and ρ_0 are the total charge of the ring, the radial and vertical displacement of the observation point from the center of the ring, and the electric permittivity in vacuum, respectively. K is the elliptic integral of the first kind. Then we summed up the contributions of the ring charges at each observation point. The number of the stacked rings was increased until the final summation converged.

As shown in the charge distribution models and the corresponding electric potential computation results shown in Fig. 3.7a, b, such a center peak appears when a ring or annular strip-shaped charge distribution is dipped or penetrated by an AFM probe's tip and it becomes increasingly higher as the charge distribution becomes more concentrated around the nanocup's rim, reducing L_{ch}. In contrast, the peak becomes much lower in the case of a half-dome charge distribution (

$L_{ch} = 0.5L_{tot}$) and almost disappears in a uniform dome charge distribution ($L_{ch} = L_{tot}$). Jacobs et al.[3] observed "dip-in-the-peak" potential profiles, the inverse of our "peak-in-the-well" profile, from their positive ring charges.

In Fig. 3.3a, the average ratio between the center peak height and the potential well depth was ~ 0.46 with the average potential well depth at 6.9±0.7 (s.d.) V. As shown in Fig. 3.7e, the best match was obtained when the tribocharge was configured to form a ∼55 nm-wide annular strip ($L_{ch} = 0.18 \cdot L_{tot}$) around the rim. Under the assumption that the tribocharge is distributed in a bipolar mosaic form [32, 80, 81, 82, 83, 84] with the overall polarity determined by the net charge, the corresponding net surface charge density is approximately -9.9 mC m^{-2} or 0.6 net negative elementary charges per 10 nm^2, which is in order-of-magnitude agreement with the result reported by Baytekin et al. (1 net negative elementary charge per 10 nm^2) for the same material combination (PDMS-PC) [1]. The fact that the potential stayed below the rim level throughout the PDMS nanocup's cavity strongly suggests that any portion of the PDMS nanocup not covered by the negative charge was uncharged or positively charged at a negligibly low charge density. Either way, our model of negative ring charge prevails.

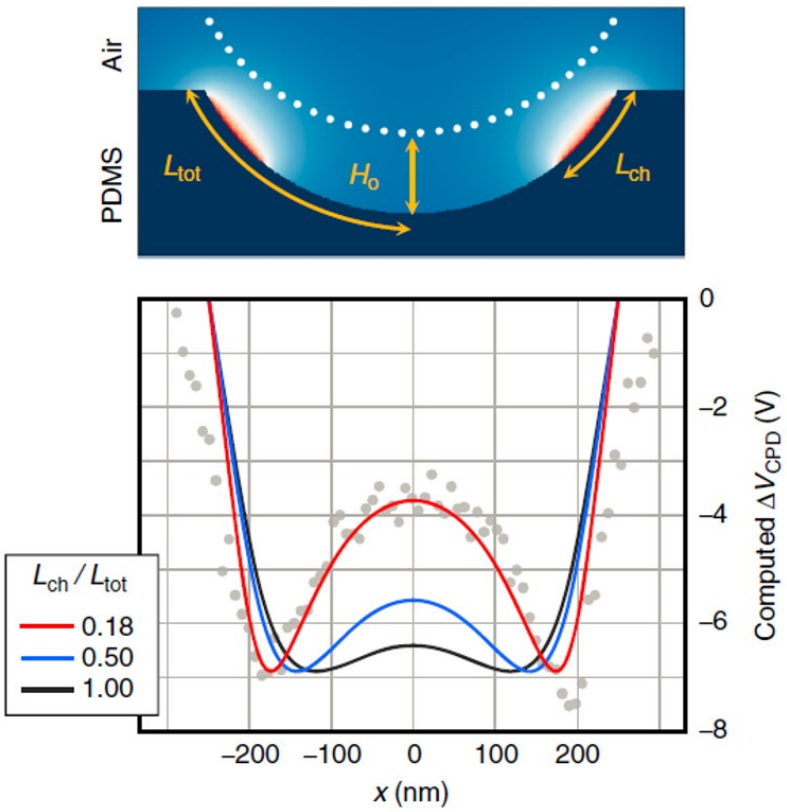

Figure 3.7 **d** A schematic diagram of the surface potential computation setup. L_{tot} and L_{ch} represent the arc lengths measured from the nanocup's rim to the bottom and the end point of the surface charge distribution, respectively. H_0 is the vertical gap maintained between the probe tips and the PDMS surface. The white dots represent the probing points for the surface potential measurement and evaluation. **e** The computed surface potentials for different charge distributions. They clearly show that the center peak rises within the potential well as the charge distribution becomes concentrated around the rim. In contrast, a dome charge ($L_{\text{ch}} = L_{\text{tot}}$) produces negligible center peak. The gray dots represent the experimental data in c within the 1.2 μm $< x <$ 1.8 μm range

CHAPTER 4. FINITE ELEMENT ANALYSIS OF REPLICA MOLDING PROCESS

From the previous chapter, we know that the shape of the generated nanopatterned surface charge from replica molding is highly dependent on the mold's nanotexture. It's reasonable to conjecture that different nanotextures generates different friction patterns in the replica molding process, which are then translated into congruent tribocharge distributions, for example, rings, partial eclipses, and dumbbells. In this chapter, we present the finite element analysis of the replica molding process. We start with the introduction of the cohesive zone model to simulate the demolding action realistically by including both vertical lifting and lateral cracking. We then build up a mechano-triboelectric model for the nanoscale elastomeric contact electrification, which remains valid all the way down in the sub-10 nm regime. The EFM is also implemented to complement the established mechano-triboelectric model.

4.1 Simulation of the Vertical Lifting

Given the supporting evidences for the ring charge formation due to the replica molding of PDMS nanocup replicated from PC nanocones, we sought the reason for such a spatially selective, non-uniform tribocharging. Our immediate hypothesis was that the PDMS nanocup's rim area sustained the highest level of friction during the demolding process which, in turn, increased the level of tribocharging in that region. To test the hypothesis, We performed a computational simulation to estimate the non-uniform distribution of the maximum frictional stress over the interface between the PDMS replica and the PC mold. Since the goal was to elucidate the spatiotemporal evolution of frictional stress on the spherical interface, we adopted the continuum-based nonlinear finite element analysis based on the cohesive zone model (CZM). All computational simulations were conducted on ANSYS (Release 18.2). We scaled up the nanocup structure to the micrometer length scale

while preserving all the geometric features due to the length-scale limit of the continuum-based FEA program in ANSYS. The material and failure characteristics of the interface elements were modeled from literature [85, 86, 87, 88]. In particular, the Young's modulus and the Poisson's ratio were set to 1.8 MPa and 0.45, respectively. The CZM was defined with 15 kPa for the normal and shear strengths and 330 μm for the separation limit. We assumed a clear interfacial failure without any fracture of PDMS fibrils, based on the observation that the PC mold stayed usable and no PDMS fracture has been detected after repeated molding/demolding.

4.2 Results of the Vertical Lifting Simulation

Due to the spherical shape of the PDMS-PC interface, the detachment occurred in a "mixed" mode, which combines the pure crack opening and the sliding modes. So, to compute σ_{f}, the frictional stress measured in Pa, we adopted the mixed mode cohesive zone model (CZM) in the presence of the nonlinearities both in material and geometry. Figure 4.1a-c shows that as the PDMS nanocup is gradually detached from the PC nanocone, the rim area experiences the maximum level of frictional stress.

To assess the cumulative impact of the frictional stress, we also computed the frictional fracture energy G_{f}, measured in J/m^2, by integrating the area under the frictional stress-tangential sliding curve over the whole process of demolding and plotted it in as a function of L/L_{tot} in Fig. 4.1d, where L and L_{tot} are the arc lengths from the nanocup rim to the observation point and the nanocup bottom, respectively, as shown in the inset. It confirms that the cumulative frictional stress during the demolding process is concentrated near the rim, forming a peak covering up to $L \sim 0.2L_{\mathrm{tot}}$, or ~60 nm in our nanocup setup, before decaying rapidly. It agrees well with our electrostatic modeling result which indicated that the surface charges formed a 55 nm-wide annular strip from the rim. Over the mid-to-bottom portion of the PDMS nanocup, the lack of intense frictional stress is likely to lead to a matching lack of tribocharging, rather than charging at the opposite polarity which will only weaken the EHDL efficiency. This analysis result not only gives

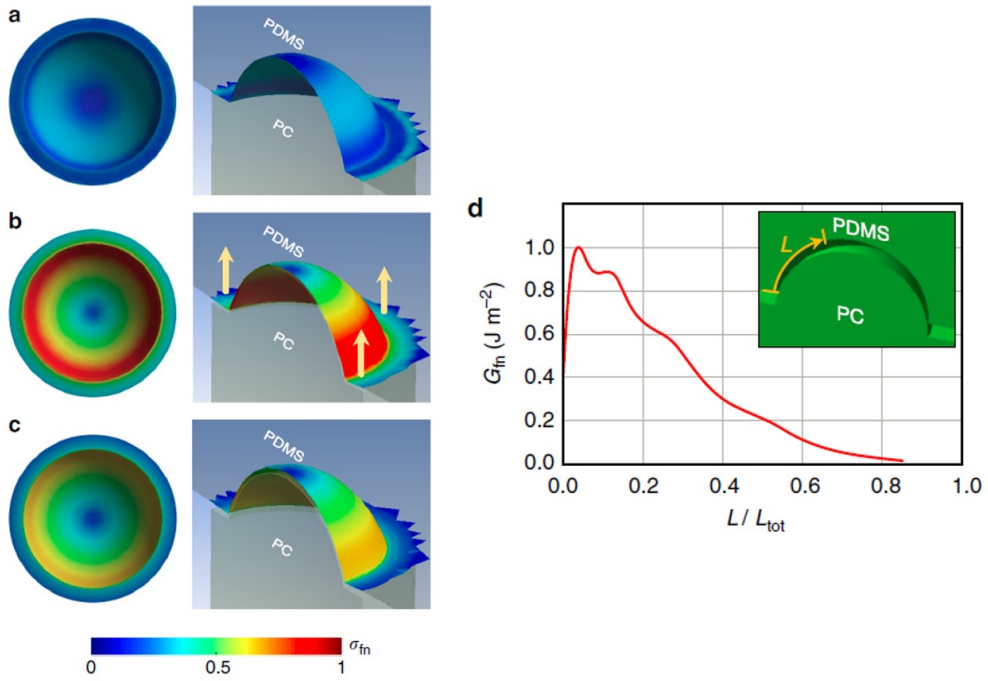

Figure 4.1 Computational analysis of demolding-induced friction. **a-c** The distribution of the frictional stress computed by nonlinear FEA. The left and right columns represent the top and cross-sectioned bird's eye views of a PDMS nanocup getting demolded from a PC nanocone, respectively. The color indicates σ_{fn}, the frictional stress normalized by its overall maximum. **a**, **b**, **c** Describe the PDMS nanocups in conformal contact with the PC nanocone, at the initial stage of the vertical demolding (along the direction indicated by the arrows), and at the starting point of the peel-off, respectively. The latter two clearly show that the demolding action induces the highest level of frictional stress around the nanocup's rim.

further corroboration to our ring charge hypothesis but also provides useful insights for designing more elaborate replica molding-based tribocharge nanopatterning.

4.3 Simulation of the Lateral Cracking

In the simulation of lateral cracking, the interface was initially assumed to be perfectly bonded and then smoothly detached by incremental displacements. Each step generates tractions based on the current interfacial displacements. For the stability of the computation, we adopted a pure

penalty mechanism and displacement-controlled CZM simulation in which a large penalty term is numerically imposed to ensure stable, smooth debonding. Thus, the interfacial displacements, not external forces, act as the primary control factor.

In particular, the displacement loading applied during the interfacial separation results in a combination of tractions in the interface-normal and interface-tangential (or lateral) directions, to be denoted as τ_{n} and τ_{t}, respectively. In the mixed-mode bilinear CZM, which we adopted for this work, the traction in each direction is related to the displacements of the interface by the damage-tracking relation as:

$$\tau_i = K_i s_i \left(1 - D_m\right), \quad (i = n, t) \tag{4.1}$$

where K_i is the cohesive stiffness. D_m is the damage parameter depending on the effective displacement jump $\lambda(t) \equiv \sqrt{\left(\frac{s_n}{s_n^c}\right)^2 + \left(\frac{s_t}{s_t^c}\right)^2}$ at time t. Initially $D_m = 0$ meaning no interfacial damage. As damage accumulates and exceeds peak (i.e., $\lambda_{\max} > \bar{s}_i/s_i^c$ where $\lambda_{\max} = \max_{\forall t}[\lambda]$),

$$D_m = \min\left(1, \frac{s_i^c}{(s_i^c - \bar{s}_i)} \frac{(\lambda_{\max} - \bar{s}_i/s_i^c)}{\lambda_{\max}}\right), \quad (i = n, t) \tag{4.2}$$

s_i and s_i^c are the current interfacial displacement and the displacement at the completion of debonding, respectively; $\bar{s}_i$ is the displacement at the peak traction.

In this way, the mixed-mode CZM relates the interfacial displacements to interfacial tractions (forces) and also to the debonding failure modes, rendering the direction of the debonding a critical parameter.

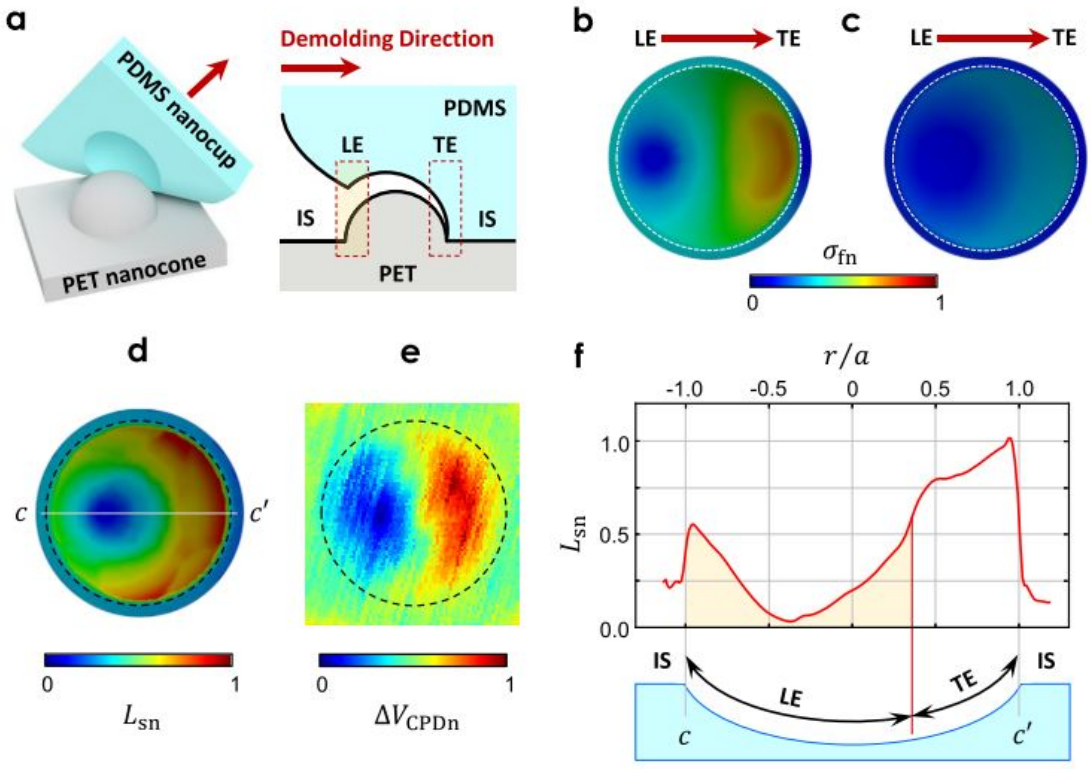

Figure 4.2 (a) Illustrations of the demolding action in bird's eye and cross-sectional views. The red arrows indicate the direction of demolding. LE, TE, and IS stand for the leading edge, trailing edge, and interstitial space, respectively. (b,c) The numerically computed distribution of the normalized frictional stress (σ_{fn}) at the initial and final stages of the demolding action in sample C, respectively. (d) Numerically computed distribution of the sliding distance (normalized to its maximum) due to the demolding action. (e) The normalized ΔV_{CPD} of one nanocup taken from Figure 3.6f. (f) The normalized sliding distance L_{sn} along the $c-c'$ path in (d). It exhibits an asymmetric check mark-curve which resembles the KPFM scans in Figure 3.6h,i.

4.4 Results of the Lateral Cracking Simulation

To verify that these complex charge patterns were also generated by the same nanotexture-dependent friction modulation process that we hypothesized for the ring-charge, we numerically simulated the nanocup/nanocone demolding action. The simulation model differed from that for sample A in imposing a lateral crack opening-type demolding initiated from one side. As shown in Fig. 4.2a, the crack opens from the leading edge (LE) on the left and propagates to the trailing edge (TE) on the right until the replica becomes fully separated from the mold. This new mode of demolding was necessary because the low aspect ratio of the nanocone appears to allow tangential sliding of one surface against the other, in addition to the vertical lifting, during the demolding. It contrasts with the case of high aspect ratio nanocones, such as sample A, in which the demolding is carried out mainly through the vertical lifting due to the high resistance to the sliding. Figure 4.2b,c shows how the frictional stress evolved during the demolding of sample C, the one with the lowest aspect ratio, from its PET mold. The inclusion of the lateral crack opening clearly concentrates the frictional stress on the TE side. The resulting breakdown of the reflectional symmetry within the nanocup agrees qualitatively with the experimentally observed asymmetry in Figure 3.6e,f.

The computed frictional stress patterns in Figure 4.2b,c, however, do not precisely match the features of the measured surface potential distribution shown in Figure 3.6f in detail. In particular, the sharp cusps in the TE area and the high contrast between the LE and TE areas clearly shown in Figure 3.6f are missing in Figure 4.2b,c, respectively. Such a mismatch is inevitable since the tribocharge's final distribution pattern is determined by the level of frictional stress accumulated throughout the demolding action at each point. Among many quantities that can be extracted from the simulation results, we found that the tangential sliding distance reflects the cumulative frictional stress most faithfully.

For facile comparison, we plotted the distribution of the tangential sliding distance, normalized to its maximum, in Figure 4.2d, and juxtaposed the normalized potential distribution, extracted from the KPFM scan of a single nanocup in sample C,as Figure 4.2e. They exhibit an improved level of similarity, especially in the salient features mentioned above, confirming the tangential

sliding distance as the key factor that can be used to predict the charge distribution pattern in the nanoscale elastomeric CE.

To obtain more information, we extracted from the simulation result the normalized tangential sliding distance L_{sn} along the centerline $c-c'$ in Figure 4.2d and plotted it in Figure 4.2f along with a schematic diagram of the PDMS nanocup. The plot reveals an asymmetric check mark (✓)-shaped L_{sn} distribution inside a nanocup that can be qualitatively explained by our nanotexture-dependent friction modulation hypothesis: During the lateral crack opening- dominated demolding of low aspect ratio nanocones, the completely flat interstitial space (IS) outside the nanocup experiences a moderate, mostly uniform level of tangential sliding which forms the pedestal at $0.25 < L_{sn} < 0.5$ in Figure 3f. Once the demolding action reaches the leading edge of the nanocone, the replica and mold becomes separated rapidly, as illustrated schematically in Figure 4.2a, without involving much tangential sliding. In accordance, L_{sn} also drops rapidly from the IS-level, almost reaching zero at the center of LE, and then gradually increases as the crack opening approaches the peak of the nanocone and passes it. In contrast, TE experiences a significantly higher level of tangential sliding as the surfaces have to brush against each other during their separation. Consequently, L_{sn} not only recovers the IS level but also surpasses it, reaching the maximal level before returning to the IS level at the edge of the nanocup (Figure 4.2f).

If the nanotexture indeed modulated the friction in accordance with the model described above and the spatially modulated friction pattern were also faithfully converted into the tribocharge distribution, then we must be able to observe the check mark-shaped asymmetric L_{sn} distribution curve inside every low aspect ratio nanocup. Inspection of ΔV_{CPD} in Figures 3.6h and 3.6i verifies that it really is the case, enabling us to affirmatively answer not only the second question but also the third, by singling out L_{sn} as the factor governing the final charge distribution pattern.

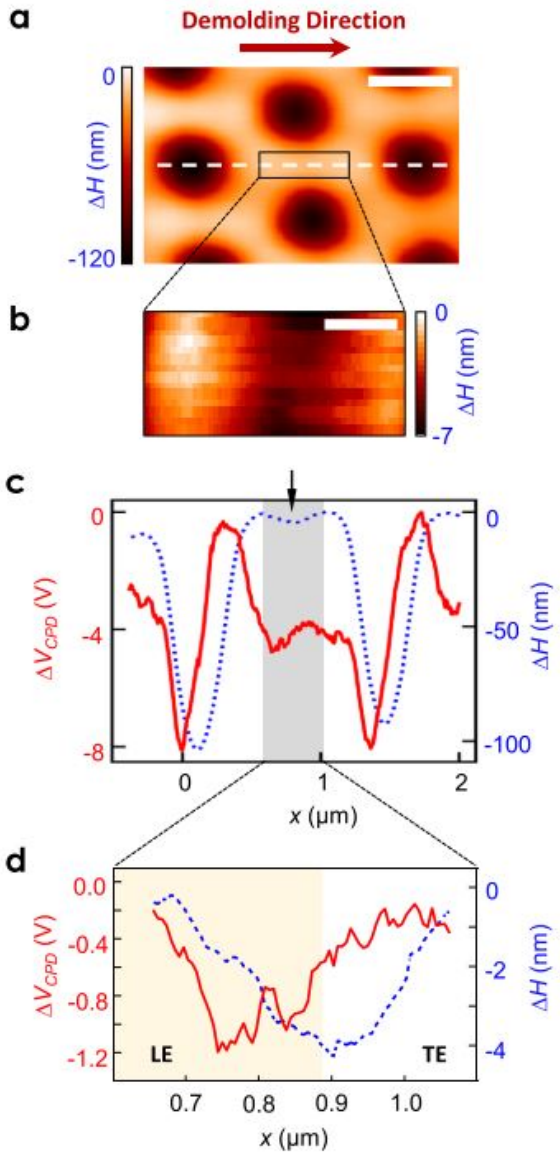

Figure 4.3 (a) Top-view topography of sample B nanocups (scale bar: 500 nm). (b) A sub-10 nm scale dip exists at the center of the interstitial area (scale bar: 150 nm). (c) AFM (dotted) and KPFM (solid) scans along the white dotted line in (a). The black down- arrow indicates the position of the sub-10 nm scale dip. (d) Magnified plots of ΔH and ΔV_{CPD} within the shaded region of (c).

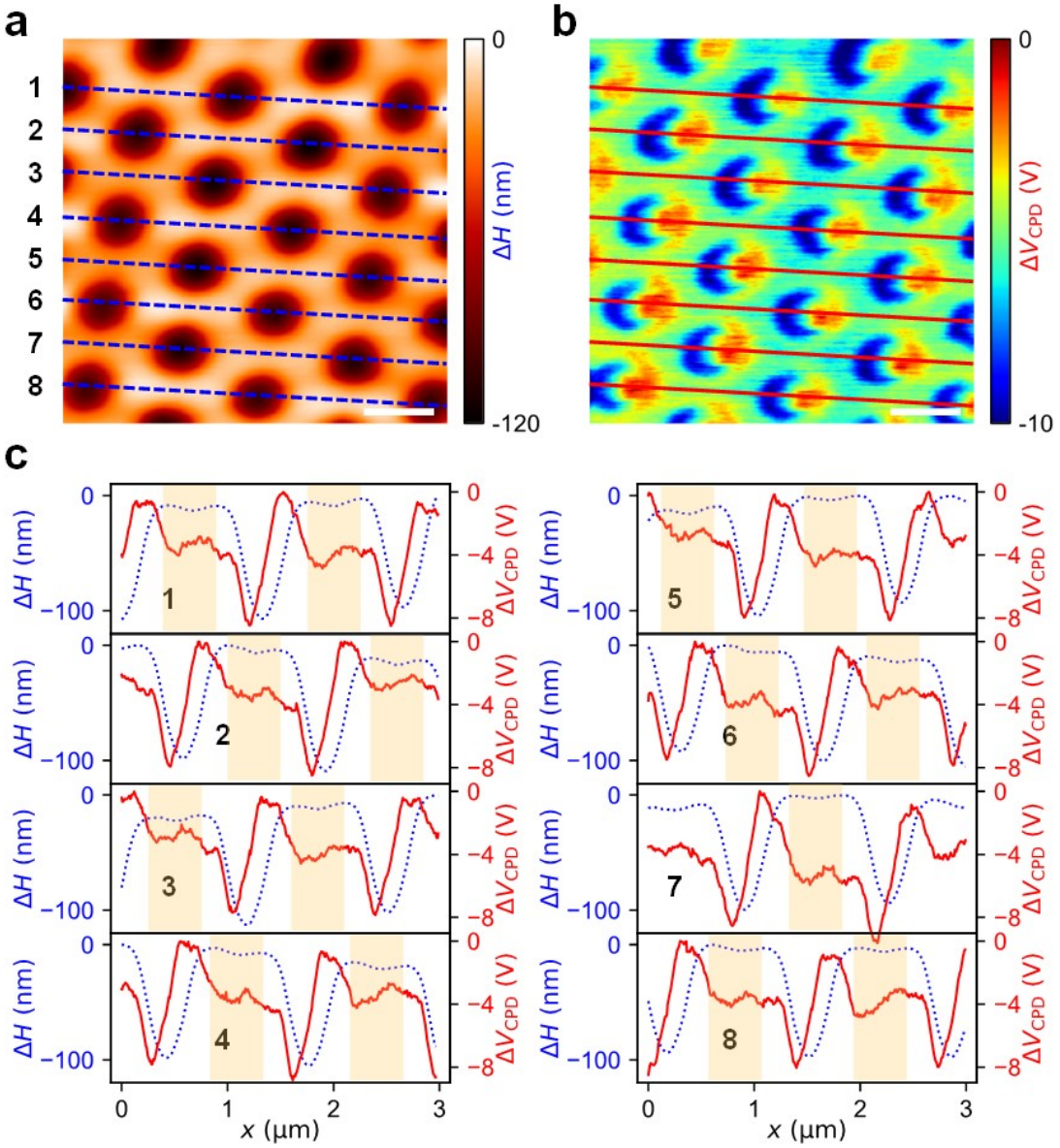

Figure 4.4 (a) The topography and (b) the corresponding potential distribution scanned over a 3×3 μm^2-wide PDMS surface. Their profiles along the long diagonals of the triangular lattice, which contain the ∼4 nm-deep recesses, are retrieved and superimposed in (c) for facile correlation. Inside the 16 recesses, most surface potential profiles exhibit the characteristic "asymmetric check mark-curve", re-affirming our mechano-triboelectric charge generation model. (Scale bars: 500 nm)

4.5 Validity Range of the Mechano-triboelectric Model

To examine the range of validity of this nanotexture- controlled friction modulation and tribocharge patterning model, we set a sub-10 nm-scale nanotexture as our next target. The AFM scan in Figure 4.3a shows that ∼4 nm-deep recesses appear at the midpoints of the triangular nanocup array's long diagonal. For the one in Figure 4.3b, the aspect ratio is only 0.027, which renders the region between the nanocup almost flat. We took KPFM scans along the dotted line in Figure 4.3a and plotted it in Figure 4.3c,d in superimposition with the surface topography.

Inside the two ∼100 nm-deep nanocups, the potential changes exactly in agreement with the hypothesized model, exhibiting the characteristic check mark-curve between the intermediate pedestal level at $\Delta V_{\mathrm{CPD}} \sim -4$V. More remarkable is the appearance of a very similar check mark-curve inside the ∼4 nm dip, as shown in magnified spatial scale in Figure 4.3d. It indicates that spatially varying CE can occur even at near-flat interfaces during their separation. Figure 4.4 shows that this nanoscale CE phenomenon is repeated in all the 16 shallow dips within a $3\times3\ \mu m^2$ scan area. Applicability of the model to such a small and slowly varying nanotexture reinforces its validity, qualifying it as a full mechano-triboelectric model of the nanoscale elastomeric CE.

For completeness, we also tested the model's validity in a nanotexture with much greater vertical extent. We used a PET surface relief grating with its depth and pitch at 300 and 700 nm, respectively (Figure 4.5). Despite its depth, the large pitch ensured a smooth demolding as described in Figure 4.2a. The geometry's simplicity also rendered the control of the demolding direction easier and accurate, enabling us to deliberately reverse the direction and monitor its impact. The potential scans, superimposed with the topography for facile correlation (Figure 4.5c,f), clearly reveal the asymmetric check mark-curves with their minima near the mid-LE, reaffirming the validity of our model. Furthermore, they also reveal that the reversal of the demolding direction resulted in the matching left-right flipping of the check mark-curve, which further corroborates our model.

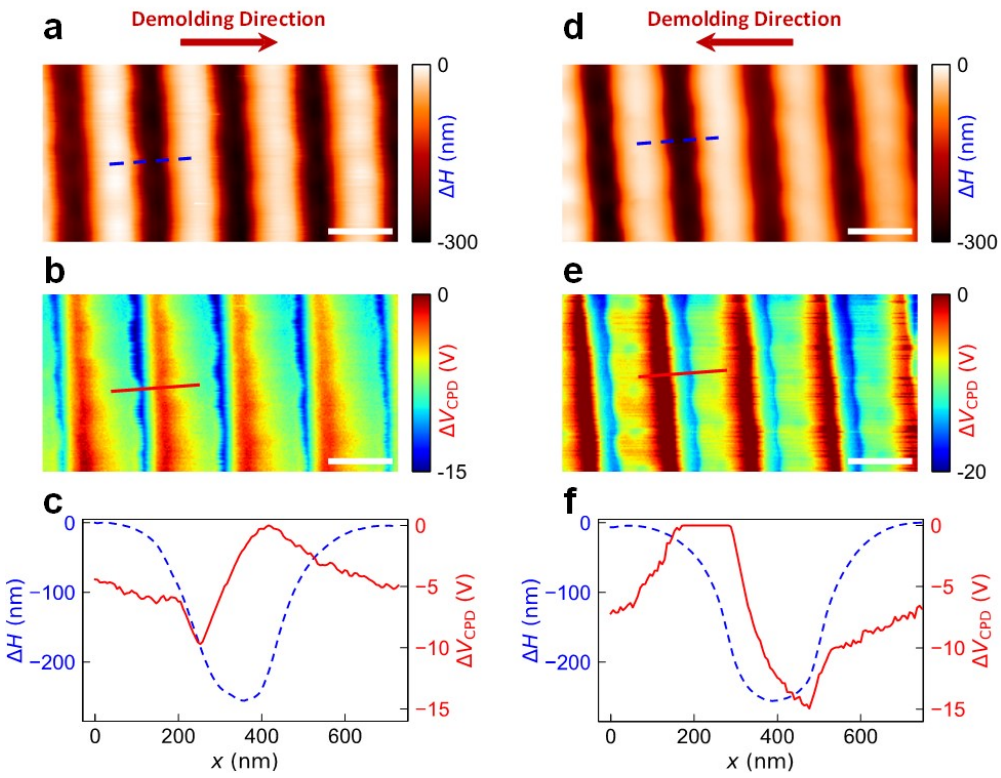

Figure 4.5 (a,d) The topography and (b,e) the corresponding potential distribution scanned over a PDMS surface replicated from a PET surface with a ∼300 nm-deep 1D grating pattern. The left and right columns differ in their direction of demolding which is indicated at the top. Their profiles along the dotted-blue and solid-red lines are superimposed in (c) and (f), respectively, for facile comparison. The surface potential is clipped at some points due possibly to use of the deeper-than-usual (∼300 nm) surface texture and denser triboelectric charge generation resulted from it. Inside the grooves, the surface potential profiles exhibit the characteristic "asymmetric check mark-curve" very similar to those shown in Figs. 3.6h, i, and 4.3d. Furthermore, the potential profiles in (c) and (f) are left-right reflected forms of each other, in full accordance with the reversal of the demolding direction. The results re-affirm our mechano-triboelectrification model. (Scale bars: 500 nm)

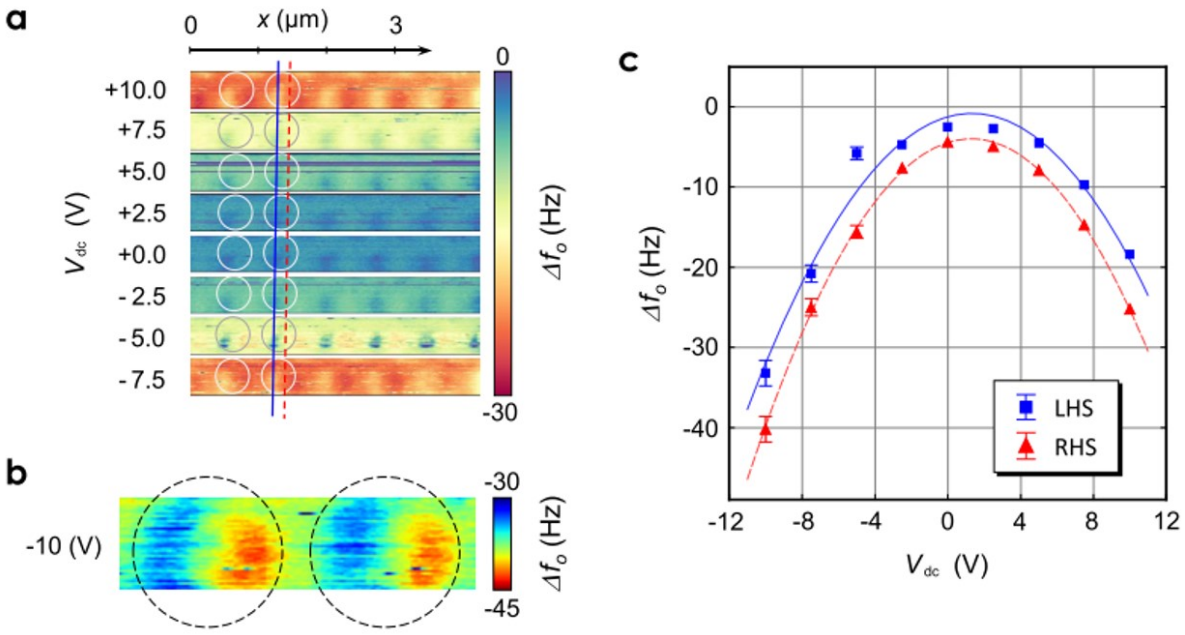

Figure 4.6 (a) EFM images of sample C under different values of $V_{\rm dc}$. A row of five PDMS nanocups were probed for the shift in the resonance frequency Δf_0. (b) A magnified EFM image at $V_{\rm dc} = -10$ V reveals the asymmetry in charge distribution. (Circle radius $a = 250$ nm.) (c) Δf_0 extracted from the left-hand side (LHS) and right-hand side (RHS) of the circled nanocup in (a) as a function of $V_{\rm dc}$. The solid and dashed curves represent the parabolic curve fitting results. The error bars represent the standard deviation obtained from five samples. Error bars smaller than the symbols were omitted for visual clarity.

4.6 Electrostatic Force Microscopy

For a more quantitative validation of the mechano-triboelectric model, we refined the charge characterization technique. The issue is that PDMS is an insulator without a clearly defined Fermi level. Since KPFM relies its operation on the Fermi level difference, the electric potential measured on insulators becomes strongly affected by the sample preparation and/or the measurement setup

[89, 90], making direct determination of the strength and polarity of the measured potential very difficult [91]. The relatively large thickness of the PDMS replica (> 1 mm) aggravates the difficulty [92]. To address these issues, we adopted EFM which has been widely used for charge characterization on insulators such as epoxy resin [72], nanocomposite [13], and adatoms [10]. By tracking the electrostatic force generated by the surface charge, EFM can directly measure the charge's polarity and density even on highly insulating substrates [73, 11], complementing the results of KPFM.

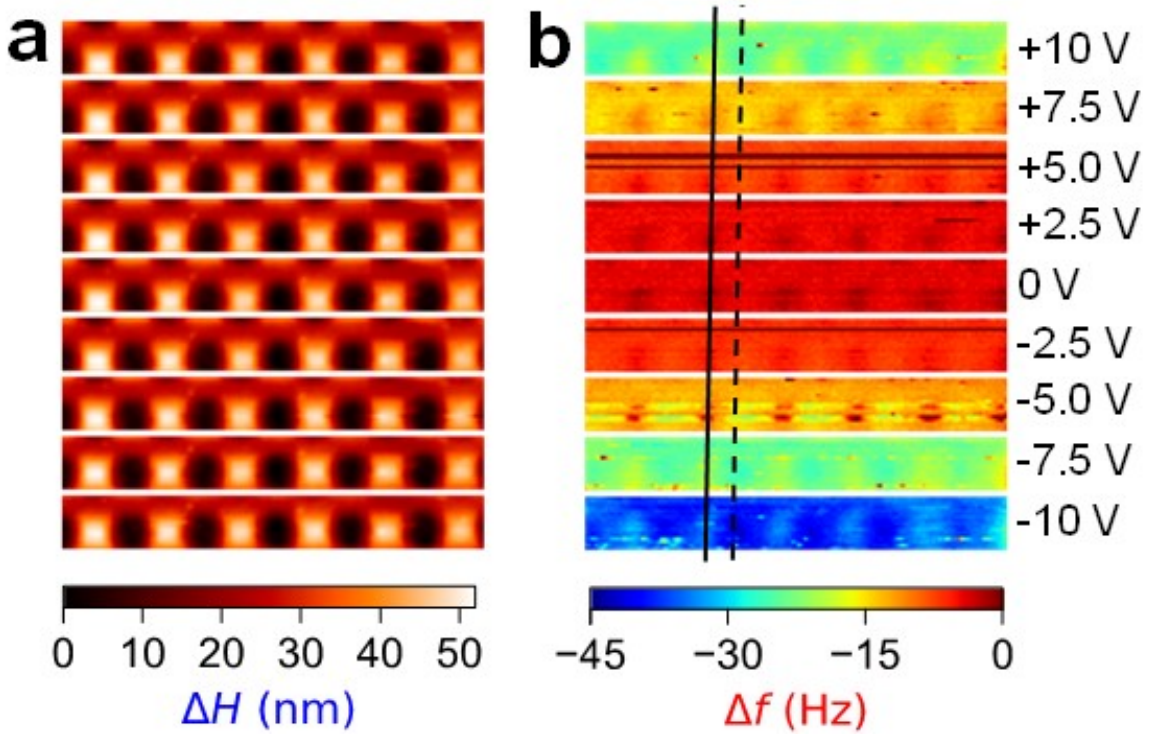

Figure 4.7 The topography (a) and corresponding frequency shift (b) with varying DC bias applied to the probe. The topography shows no significant variation other than the slights shift caused by the scanning drift. In contrast, the frequency shift varies considerably, showing a quadratic dependence on the applied DC voltage.

We conducted EFM on five PDMS nanocups in sample C. Figure 4.6a shows the resonance frequency shift at varying values of V_{dc}. We found that the topography images exhibited no significant variation other than slight shifts caused by the scanning drift (Figure 4.7a). In contrast, Δf_0 shifted considerably as a quadratic function of V_{dc}. Figure4.6b shows the map obtained at $V_{\mathrm{dc}} = -10$ V in a magnified view. It is clear that the frequency shift within a single nanocup exhibits an asymmetric dumbbell pattern.

To quantify the difference in the surface charge, we plotted the frequency shifts in the left-hand and right-hand sides of nanocups as a function of the applied probe bias, as depicted in Figure 4.6c. The solid and dotted lines were the quadratic fitting to the data, with the maxima at 1.33 and 1.29 V in the left-hand side and right-hand side, respectively. The frequency shift at zero bias ($V_{\mathrm{dc}} = 0$) was measured to be -1.3 and -4.5 Hz.

From eqs 2.10 and 2.11, the surface charge was determined to be positive and the absolute value was 0.015 and 0.028 elementary charges per 10 nm^2. In the estimation, we assumed that the electrostatic coupling between the probe's tip and the surface occurred over an area of 10^4 nm^2, a typical value [72] which also is approximately the area of the blue circle in Figure 4.6d. From the subduplicate ratio between the Δf_0 values, it was estimated that the surface charge density in the right (TE) side was $\sqrt{4.5/1.3} \approxeq 1.86$ times higher than that in the left (LE) side. This difference in the charge density within a single nanocup is consistent with the surface potential patterns shown in Figure 3.6f. To quantitatively relate this tribocharge density ratio to the difference in the sliding distance experienced by the LE and TE areas, we integrated the areas under the LE (shaded) and TE (plain) portions of the normalized L_{sn} curve in Figure 4.2f. The ratio turns out to be approximately 1.98 which is very close to the charge density ratio obtained above. This result indicates that the sliding distance can be linearly related to the induced tribocharge density and corroborates the mechano-triboelectric model quantitatively.

CHAPTER 5. ELECTROHYDRODYNAMIC NANOLITHOGRAPHY WITH NANOPATTERNED SURFACE CHARGE

This chapter presents an exemplary application of the nanopatterned tribocharge generated from the replica molding process, that is, the electrohydrodynamic nanolithography (EHDL). The main idea is to utilize the nanopatterned tribocharge as the source of the spatially-modulated electric field to polarize the polymer film. We start with an overview of the conventional EHDL methods, followed by an introduction of the our strategy for the EHDL process. The second and third sections describe our proposed tribocharge-enable EHDL process in detail. The results and numerical modeling of the EHDL process are then further discussed in collaboration with the previous surface charge characterization. Finally, we describe a nanolens shape control method inspired from the EHDL process.

5.1 Overview of Conventional EHDL Process

Electrohydrodynamic nanolithography (EHDL) is a polymer thin film patterning technique utilizing the electrohydrodynamic instabilities [14, 15]. The electric field drives the polymer film to form micro- or nano- scale patterns. In 1999, Chou and Zhang reported the lithography-induced self-assembly [14], in which periodic arrays of pillars were formed from a originally flat thin film. As shown in Fig. 5.1, a thin layer of polymer film is first spin coated on a silicon substrate. Then a top mask with protruding patterns is placed above the polymer film, with a certain distance determined by the spacer used. No external electric field is applied. The polymer film is then heated above its glass transition temperature (T_g) to enable the formation of micro- and nano-structures via the electrohydrodynamic instability. The whole system is then cooled down quickly to room temperature to freeze the formed patterns.

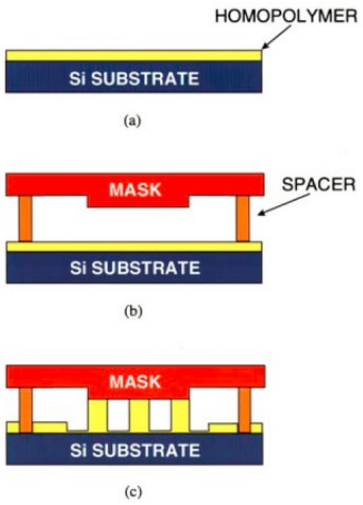

Figure 5.1 Schematics of the lithography induced self-assembly. Adapted from [14].

Figure 5.2 shows the optical graph and AFM image of the multi-domain closed-packed hexagonal PMMA pillars formed using a mask with flat surface. In addition, many other patterns can be formed with different shapes of protrusion on the top mask, for example, lines [15], squares [93], rectangles [14], triangles [94], and rings [95]. This EHDL process is attractive once being invented thanks to the advantage that the top mask is a flat and doesn't have to be pre-patterned compared with many other lithography methods. However, the origin of the electric field remain elusive. It's suggested that the electric field is likely from the trapped charges in polymer film or a thin layer of thermally grown silicon oxide [96].

The EHDL process is also possible by applying electric field externally [15]. Figure 5.3a shows the polymer film in between a flat top electrode and bottom electrode with external voltage applied. The microstructures are formed due to the polymer instability. In Fig. 5.3, however, the top electrode is topographically patterned so that the polymer instability occurs first in locations with the smallest gap between the electrode and the polymer film. This leads to a positive replication of the top electrode, as shown in Fig. 5.4.

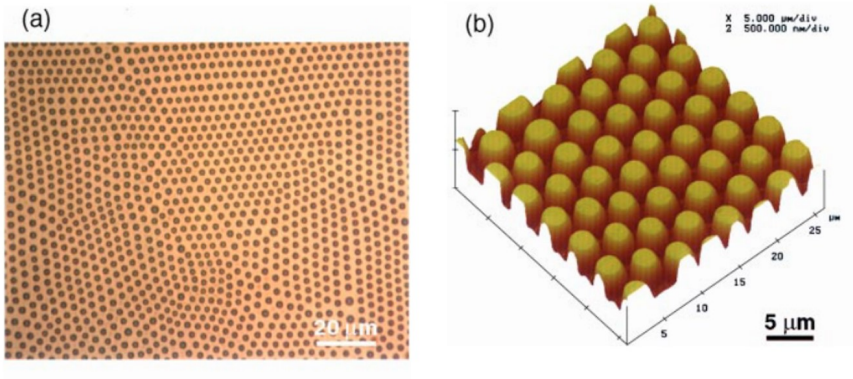

Figure 5.2 (a) Optical and (b) AFM image of the periodic polymer pillars array formed in the lithography induced self-assembly. Adapted from [14].

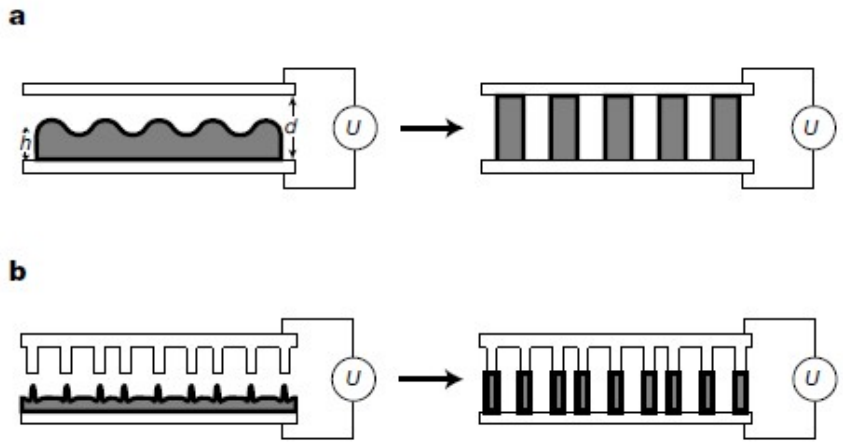

Figure 5.3 (a) The external voltage applied leads to the polymer instability to form microstructures in between the top and bottom electrode, similar to the lithography induced self-assembly. (b) The top electrode is topographically patterned so that the polymer instability happens first at the locations with the smallest gap. This leads to a positive replication. Adapted from [15].

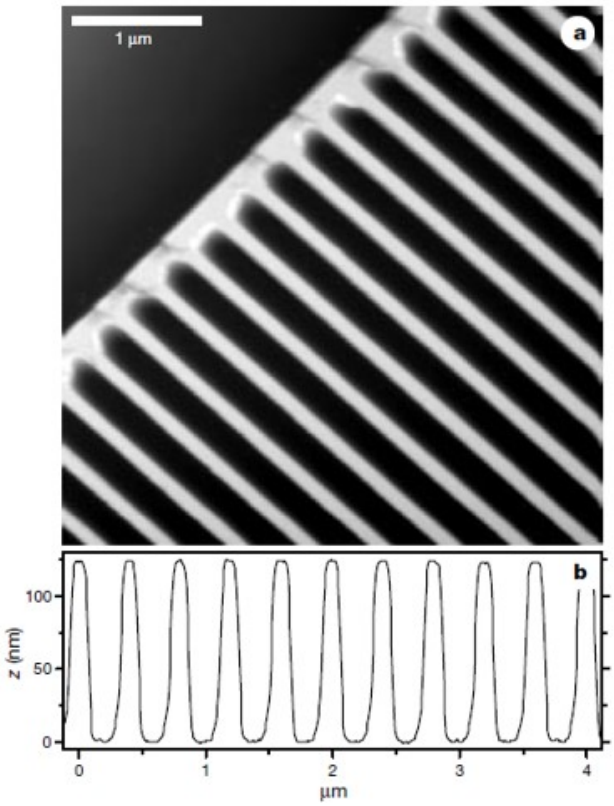

Figure 5.4 (a) The AFM image of the patterned grating structure corresponding to the scheme in Fig. 5.3b. (b) The cross sectional scan shows a step height of 125 nm. Adapted from [15].

5.2 Surface Pre-texturing for Tribocharge-enabled EHDL

In EHDL, liquid-phase polymer becomes polarized and attracted by spatially modulated electric fields and forms out-of-plane structures upon solidification [14, 97, 15, 96, 98]. Therefore, the gap between the source of the electric field and the polymer surface is one of the most important factors in EHDL. Conventional EHDL utilizes a patterned electrode as the source of the electric field and separately prepared dielectric thin film stripes as the spacers [14, 99]. Here we utilized the tribocharged PDMS nanocups (Fig. 5.5a) as the source of the electric field. To place a gap between them and the polymer surface, we selected a photopolymer, which undergoes low but definite volume shrinkage upon exposure to UV irradiation [100], as the EHDL's target material and then textured the surface with a spatially modulated UV beam. The recesses in the resulting texture provide the gaps.

Specifically, the UV-curable photopolymer (NOA73, Norland Inc.) was spin-coated on the silicon substrate for 10 s at 500 r.p.m. and then 45 s at 3000 r.p.m., resulting in a thin film with thickness of $\sim$ 40 μm. The photopolymer thin film was then exposed to a UV-two-beam interference pattern (Fig. 5.5b) generated by the Lloyd mirror set-up employing a HeCd laser (Kimmon) installed on a floated optical table. The pitch can be facilely controlled by the beam incident angle. The power intensity of the interference pattern on the photopolymer thin film was around 1 mW/cm^2 (power meter, 2931-C, Newport). The dose applied to the photopolymer was controlled by the exposure time, and hence the amplitude of the obtained one-dimensional surface relief structure can be accurately tuned. Then the NOA73 surface became sinusoidally textured due to the local volume shrinkage (Fig. 5.5c). The AFM scans of two different types of sample sinusoidal textures on NOA73 are shown in Supplementary Fig. 5.6. Their profiles exhibit excellent agreements with the theoretically predicted sinusoidal pattern, signaling a successful two-beam interference. The strong crest-to-trough contrast, maintained even after several tens of minutes of exposure, also attests to the overall integrity of the Lloyd mirror setup.

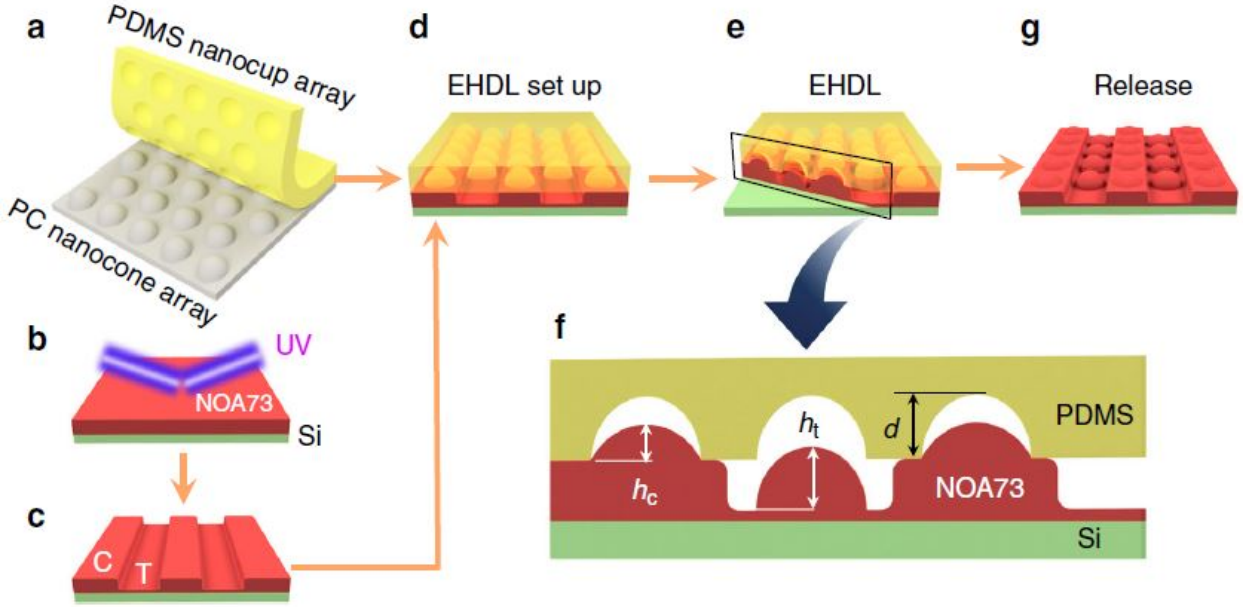

Figure 5.5 Fabrication steps for tribocharge-enabled EHDL of photopolymer. **a** Liquid-phase PDMS is poured onto the PC mold textured with a 2D triangular nanocone array. After thermal curing, the PDMS replica, textured with a nanocup array, is peeled off. Its surface becomes selectively tribocharged during this demolding process. **b** A UV-curable photopolymer (NOA73) is spin-coated on a silicon substrate and exposed to a UV-two-beam interference pattern. **c** The NOA73 thin film is textured sinusoidally with well-defined crest (C) and trough (T) areas due to local volume shrinkage. **d** The tribocharged PDMS nanocup array is placed on the sinusoidally textured NOA73 film. **e** NOA73 in the trough region is attracted upward by the spatially modulated electric fields originated from the tribocharges and undergoes EHDL. NOA73 on the crest experiences forces from both the capillary action and Coulomb attraction. **f** The cross-sectional profile defines the heights of the nanostructures in the crest (h_c) and trough (h_t) areas along with d, the nanocup depth. **g** The final UV-induced solidification of NOA73 and removal of the PDMS nanocup array completes the tribocharge-enabled EHDL of NOA73

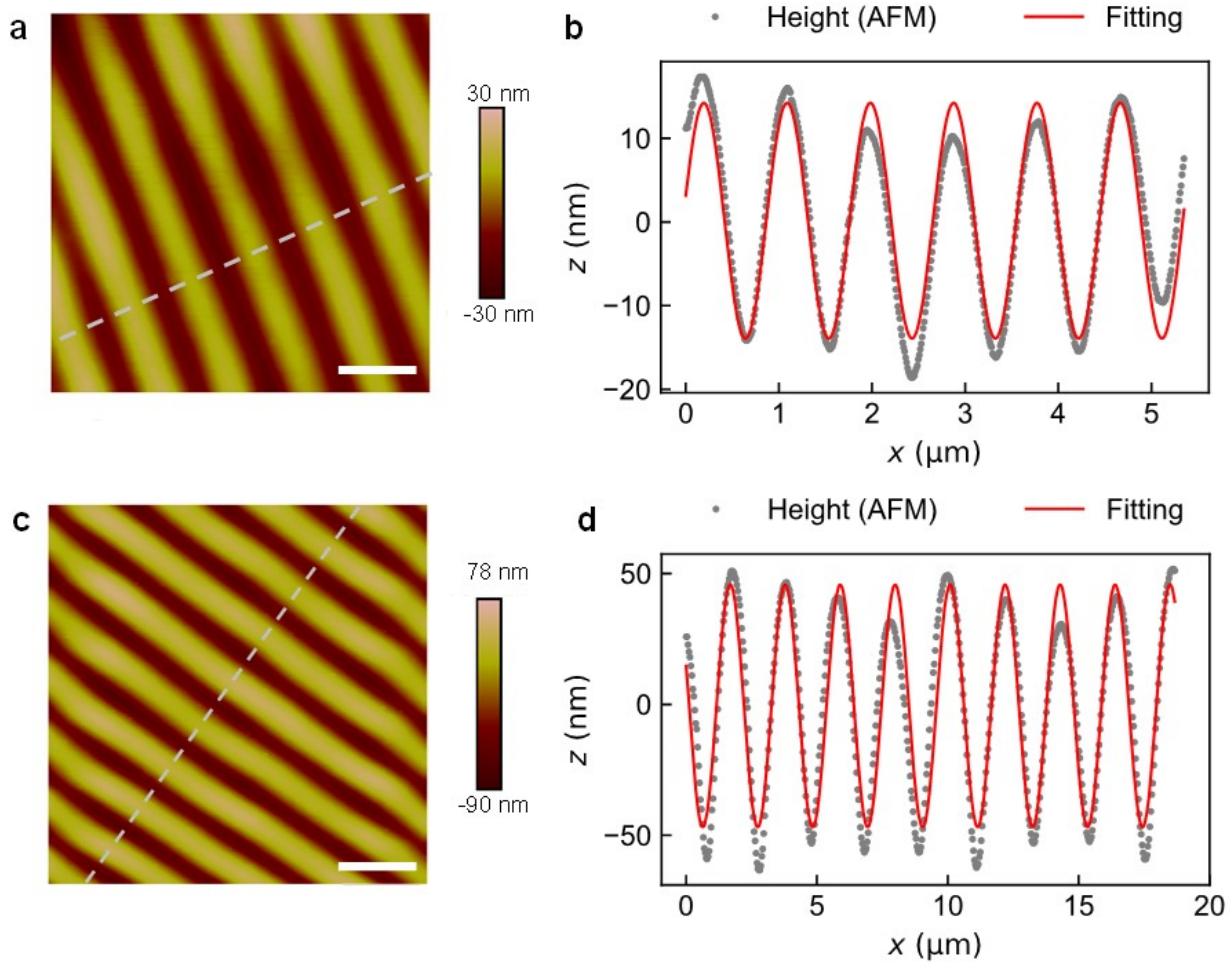

Figure 5.6 Morphology of UV-induced sinusoidal texture These atomic force micrographs show the morphologies of the UV 2-beam interference-induced sinusoidal textures made on NOA73. **a** and **b** show the top and profile views of a texture with 900 nm pitch (10 degrees tilt angle in the Lloyd mirror setup) and 29±2.7 nm in depth. The dose and exposure time were 1.6 $J \cdot cm^{-2}$ and 60 mins, respectively. **c** and **d** are from another texture with 2.1 μm pitch (2 degrees tilt angle) and 99±11 nm in depth. The dose and exposure time were 2.2 $J \cdot cm^{-2}$ and 80 mins, respectively. The laser intensity was $\sim 0.45 mW \cdot cm^{-2}$. In **b** and **d**, the red solid curves represent sinusoidal fitting results, which confirm the sine-squared-nature of the interference intensity pattern in Lloyd setup.

Note that even though the NOA73 thin film's inner volume becomes well cured by the UV exposure [101], a thin layer at its top surface remains fluidic and, hence, available for EHDL due to the oxygen-induced inhibition of photopolymerization [102, 103, 104]. When the tribocharged PDMS nanocup array was placed on the pre-textured NOA73 film (Fig. 5.5d), the troughs of the sinusoidal texture provide periodic recesses in which the NOA73 surface is vertically separated from the tribocharges by a submicron-scale gap.

Providing vertical separation through UV-induced texturing of the target material itself, rather than by adding heterogeneous spacers [14, 99], leads to an additional merit. As illustrated in Fig. 5.5e, f, the crest portion of the sinusoidally textured NOA73 is in direct contact with the tribocharged PDMS nanocups and, hence, experiences both capillary action and tribocharge's Coulombic attraction. On the other hand, the trough portion, which is vertically separated from the tribocharged PDMS surface, experiences only the Coulombic attraction. This fact will prove useful in analyzing the EHDL results to corroborate the ring charge hypothesis.

5.3 Tribocharge-enabled EHDL

Upon completion of the photopolymer surface pre-texturing, we carried out the EHDL process. As shown in Fig. 5.5d-g, we placed the tribocharged PDMS nanocup array on the sinusoidally textured NOA73 thin film, left it for a preset period of time, and then applied the final UV irradiation to fix the final shape. The completely cured NOA73 film was peeled off from the PDMS surface and then examined by AFM.

Three different UV doses, 1.2, 1.8, and 3.6 J/cm^2, were used for the two-beam interference to produce different gap widths between the tribocharge and the NOA73 surface. AFM scans of the resulting three samples, to be referred to as Samples A, B, and C, are shown in Fig. 5.7. They reveal the impact of the UV dose on the final EHDL result. The scans from Samples A and B, shown as Fig. 5.7a, d, respectively, indicate that the EHDL process generated nanocones arrayed on the top of the sinusoidally textured NOA73 surfaces, at locations matching those of the PDMS nanocups. The absence of parasitic protrusions on the NOA73 surface between the nanocones indicates that

the flat, interstitial area between the nanocups' apertures hosted little or no net tribocharge. The nanocone array (∼750 nm in pitch) and the sinusoidal texture (∼2.6 μm in pitch) jointly constitute a two-level hierarchy which will be useful for many applications, such as superhydrophobic surfaces [105, 106].

The trough nanocones, however, cannot be unambiguously attributed to EHDL yet. Given the high-level flexibility of PDMS [107], it is possible for the PDMS nanocup array to collapse down to the sinusoidally textured NOA73 surface, make a conformal contact with it, and produce the nanocones through capillary filling of the nanocups with the liquid-phase NOA73, rather than through EHDL. We, however, reject the conjecture based on the observation that the heights of the nanocones on the NOA73 crests (h_c ∼25 nm as shown in Scan 3 of Fig. 5.7f) and troughs (h_t ∼70 nm as shown in Scan 1 of Fig. 5.7f) are very different while the capillary filling-induced nanocones must exhibit similar heights. Moreover, the height of the crest nanocones is not just different from that of the trough nanocones but actually shorter. It is almost counterintuitive given the fact that the crests of the NOA73 texture corresponds to the destructive portion of the UV-two-beam interference pattern, which leaves NOA73 more fluidic and deformable. On the other hand, the trough portion of the NOA73 texture corresponds to the constructive part which cures NOA73 more intensely. Yet, the NOA73 in the trough resulted in higher nanocones. Based on these observations, we reject the conjecture of collapsed PDMS and attribute the trough nanocones unambiguously to the tribocharge-enabled EHDL.

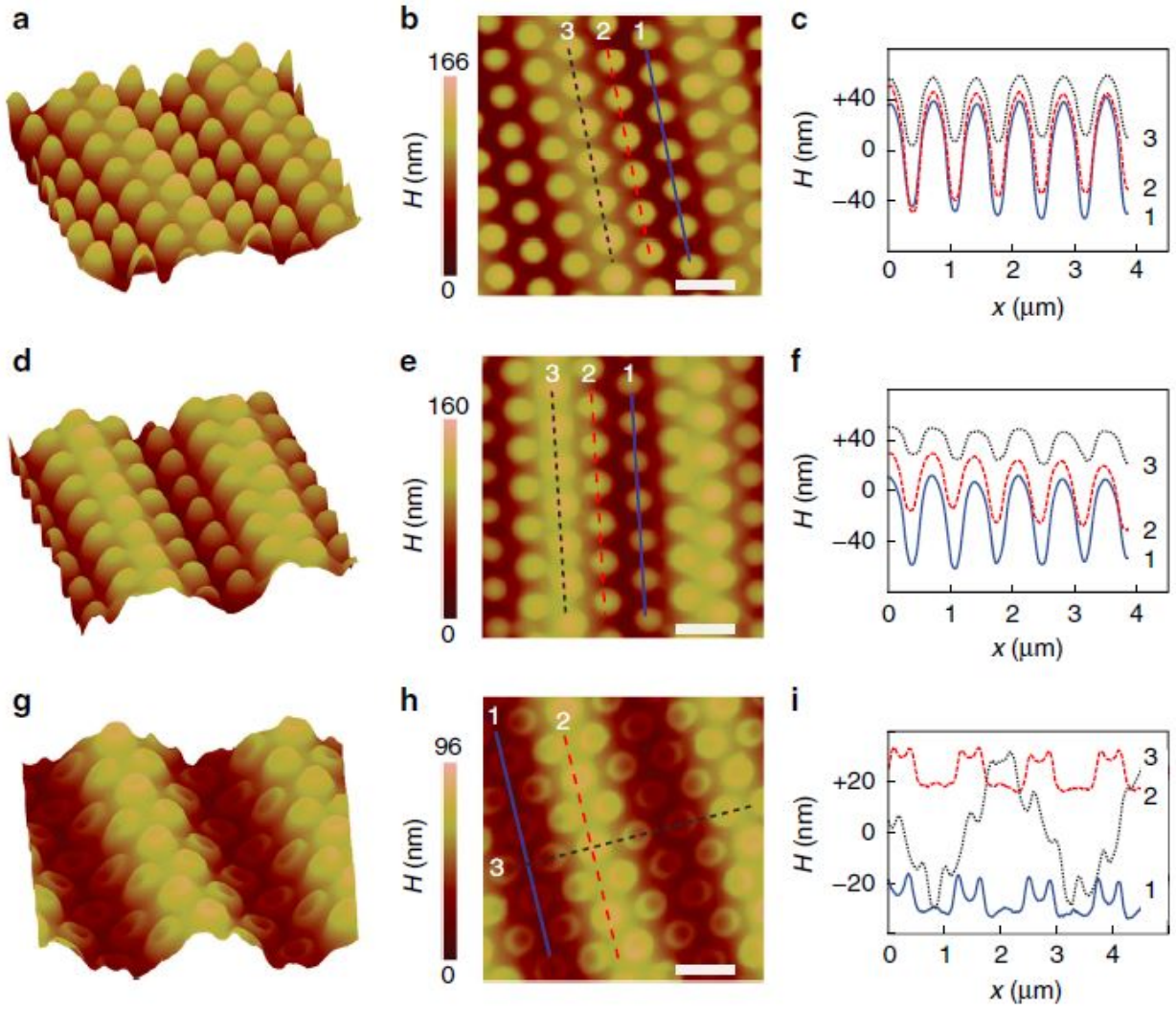

Figure 5.7 EHDL-generated nanocones and nanovolcanos. AFM scans of EHDL results obtained with the UV exposure dose of the two-beam interference lithography set to **a-c** 1.2 J/cm^2, **d-f** 1.8 J/cm^2, and **g-i** 3.6 J/cm^2. The first and second columns show the final textures in the bird's eye and top views, respectively. The third column shows their cross-sectional profiles along the lines in the second column. While the low dose, narrow-gap EHDL produced nanocone array as shown in the first two rows, the high dose, wide-gap EHDL resulted in a nanovolcano array as shown in the third row. (Scale bars: 1 μm)

5.4 Evidence of Ring Charge Distribution

5.4.1 Underfilled Crest Nanocone

The crest nanocones are more intriguing since their height is less than the depth of the PDMS nanocup (d ~153 nm). It indicates that NOA73 failed to fill the nanocup completely. It was surprising since the time required for NOA73 to fill the PDMS nanocup through capillary action is < 1 s according to [108, 109]

$$t = \frac{2\mu d^2}{R\gamma \cos\theta} \tag{5.1}$$

where μ is the viscosity of NOA73, d is the PDMS nanocup depth, R is the hydraulic radius of the nanocup, γ is the surface tension of NOA73, and θ is the contact angle between NOA73 and PDMS. In our experiments, we maintained the contact between PDMS and NOA73 for at least 2 min. Yet, the filling was incomplete. By assuming that the tribocharges were distributed only around the nanocup's rim, we can explain this underfilling as the result of the attraction from the tribocharges which pulls down NOA73 toward the rim, counteracting the capillary flow toward the inner cavity [110].

5.4.2 Nanovolcano Formation

The ring charge hypothesis can be further corroborated by the very unusual nanovolcano structures (Fig. 5.7g, h, i) produced by the tribocharge-enabled EHDL with the UV dose increased to 3.6 J/cm^2 (Sample C). Their biggest distinction from the nanocone structure is the nanocrater with 10 nm-scale height. The formation of the nanocrater indicates that NOA73 was attracted more strongly toward the rim of the nanocup's aperture than its center. If the tribocharges were distributed only along the nanocup's rim, they can attract the photopolymer in that fashion, as shown schematically in Fig. 3.1b. Under such a charge distribution, the nanocones in the troughs shown in samples A and B (Fig. 5.7a, d) can be interpreted as the result of the nanocrater's fusion at the center of the nanocup due to the lower UV dose, which renders NOA73 more fluidic and dispersive.

Note that the height profiles in Fig. 5.7 could give the wrong impression that the sinusoidal texture is deeper in Fig. 5.7 than in Fig. 5.7i even though the former sustained a lower UV dose and, consequently, smaller shrinkage and shallower texturing. It can be explained by the fact that the upward deformation of photopolymer in both EHDL and capillary filling requires additional photopolymer. Therefore the nanocones in the trough in Fig. 5.7c achieved their height by lowering the bottom level around them, thus generating the illusion of a deeper trough.

To further corroborate the ring charge hypothesis, we proceeded to reconstruct the tribocharge distribution through iterative numerical simulations in which the model charge configuration was adjusted until a good agreement was reached between the experimental and simulation results. The two-dimensional model of the experimental setup is shown in Fig. 5.8a. The simulation is based on Eq. 5.2 which describes the nonlinear electrohydrodynamic interaction between the electric field and incompressible Newtonian fluid as [111, 112, 113]

$$\frac{\partial h}{\partial t} = \frac{\partial}{\partial x}\left(\frac{h^3}{3\mu} \cdot \frac{\partial P}{\partial x}\right) \tag{5.2}$$

where x is the lateral coordinate, $h(x,t)$ the height of the polymer surface in y-direction, μ the viscosity, and t the time. P is the pressure acting on the polymer surface and typically includes three components: the Maxwell stress, the Laplace pressure, and the disjoining pressure. They result from the Coulombic attraction, the interfacial tension, and the van der Waals interaction between the polymer and the electrode surfaces, respectively. Since the disjoining force becomes significant only when the polymer gets very close to the electrode, which is not the case in our EHDL, it is excluded from the simulation.

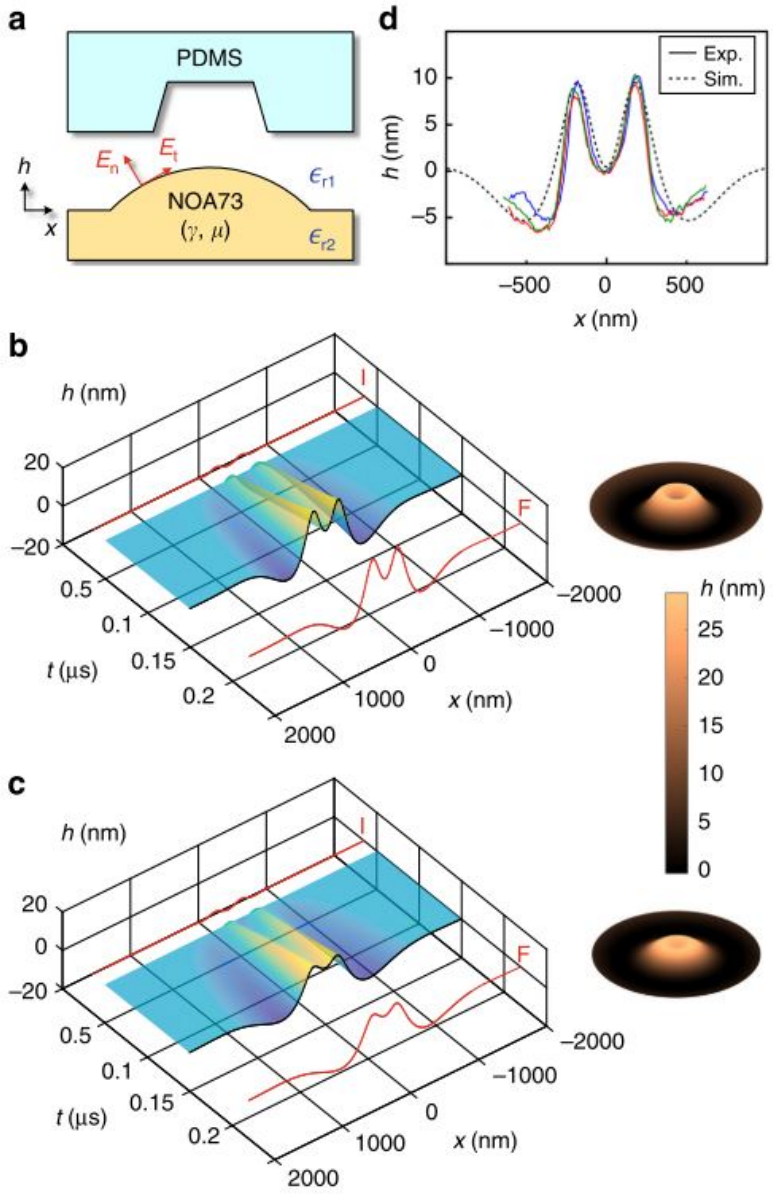

Figure 5.8 Numerical modeling of the EHDL process. **a** The 2D model for the numerical EHDL simulation. **b** The simulated evolution of the nanovolcano structure. The inset shows the revolved version of the final profile (marked as "F"). **c** The simulation result obtained after lowering the viscosity of NOA73. The nanocrater in b merged at the center to transform the nanovolcano into a nanocone. **d** The simulation (dotted line) and experimental (solid lines) results exhibit good agreements

Regarding the Maxwell stress, conventional EHDL simulations often include only the vertical, y-directed electric field [112]. Since our tribocharge-enabled EHDL setup utilizes non-uniform, highly localized charge distributions, we considered both normal and tangential electric fields at every point on the polymer surface. The overall pressure term becomes [114]

$$P = \gamma \cdot \frac{\partial^2 h}{\partial x^2} + \frac{\epsilon_0}{2}\left(\epsilon_{\mathrm{r1}}^2 E_{\mathrm{n}}^2 \cdot \left(\frac{1}{\epsilon_{\mathrm{r1}}} - \frac{1}{\epsilon_{\mathrm{r2}}}\right) + E_{\mathrm{t}}^2 \cdot (\epsilon_{\mathrm{r2}} - \epsilon_{\mathrm{r1}})\right) \tag{5.3}$$

where the first and the second terms are the Laplace pressure and the Maxwell stress, respectively, γ the interfacial tension of the polymer, $E_{\mathrm{n}}(E_{\mathrm{t}})$ the strength of the electric field normal (tangential) to the polymer surface, $\epsilon_{\mathrm{r1,r2}}$ the relative permittivity of the material, and ϵ_0 the electric permittivity in vacuum.

We solved the governing equation numerically by integrating it over time t. The parameters were set to the values that are either measured or obtained from the literature. In particular, μ and γ of NOA73 were set to 130 cps and 0.04 N/m [115]. Along the x-direction in Fig. 5.8a, the computational domain measured 4 μm and was discretized into 150$\sim$230 computation points. Along the h-direction, the extent was varied from its minimum at 100 nm, i.e., the gap between the PDMS replica and the NOA73 surfaces, depending on the shape of the charge distribution within the nanocup, which was modeled to exhibit an arc or a super-Gaussian profile. Since the simulation was carried out in 2D, the model charge distribution was configured to reproduce the 3D distribution pattern after revolution about the center axis. For example, a simple ring charge distribution was translated into two point charges located symmetrically about the center axis of the nanocup. More pairs were added to model charge distributions covering the nanocup's cavity wall. We computed the electric fields by applying Coulomb's law along the surface profile of the polymer and decomposing the result into components tangential and normal to the surface. Once the pressure term in Eq. 5.3 was evaluated, it was substituted into the right hand side of Eq. 5.2 which, in turn, got integrated in time domain using Newton-Rahpson method. The integration time was set to 5.2 ps empirically. All computations were performed with Matlab (R2013b, Mathworks Inc.).

Figure 5.5b shows the nanovolcano formation as a function of time. Again, the best agreement between the simulation and experimental results was achieved when the tribocharge distribution was set to the form of a ring around the rim of the PDMS nanocup. Figure 5.5b clearly shows that the nanovolcano initially appears as an annular ridge induced by the ring charge (marked as "I"), becomes taller and thicker, and then begins to merge at the center. At that point, the balance between the upward pulling Coulombic attraction and the laterally broadening Laplace pressure becomes critical. Depending on their relative strengths, the final state (marked as"F" can be either a nanocone or nanovolcanos with varying values of crater height. For example, Fig. 5.5c shows the simulation result obtained after the μ and γ values changed to 100 cps and 0.08 N/m [115], respectively, which corresponds to the case of low-UV-dose and less-viscous NOA73. Even though the initial profile is identical to that in Fig. 5.5b, the final profile exhibits only a small dip at the center due to the dispersion and merging of the crater at the center. By iteratively adjusting the relative strengths of the Coulombic attraction and Laplace pressure in the simulation, we could reproduce the experimental results very closely. For instance, Fig. 5.8d shows the simulated surface height profile very closely agrees with those of the three nanovolcanos (Fig. 5.7i, Scan 1).

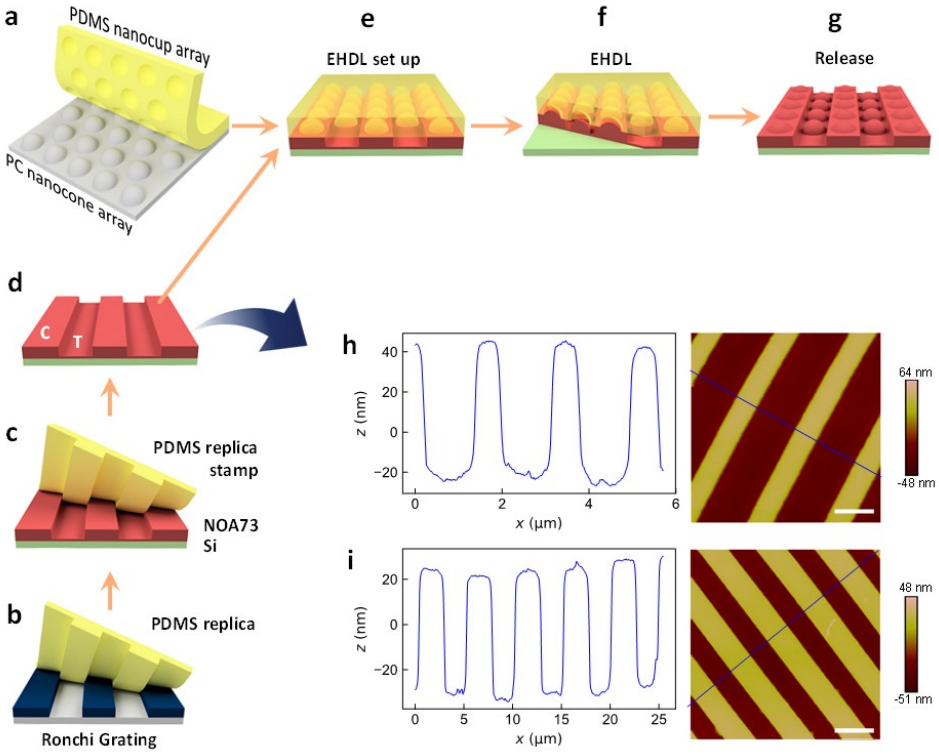

Figure 5.9 Tribo-EHDL on NOA73 surfaces corrugated through replica molding **a** Liquid-phase PDMS is poured onto the PC mold textured with a 2D triangular nanocone array. After thermal curing, the PDMS replica, textured with a nanocup array, is peeled off. Its surface becomes selectively tribocharged during the demolding process. **b** A PDMS mold is replicated from Ronchi gratings. **c** The PDMS replica is placed in contact with the spin-coated NOA73 film. **d** The PDMS replica is removed after the partial curing of the NOA73 with UV light. **e** The tribocharged PDMS nanocup array is placed on the textured NOA73 film. **f** NOA73 in the trough region is attracted upward by the spatially modulated electric fields originated from the tribocharges and undergoes EHDL. **g** The final UV-induced solidification of NOA73 and removal of the PDMS nanocup array complete the tribocharge-enabled EHDL of NOA73. **h** AFM image of NOA73 surface with a 1.7 μm-pitch linear corrugation (Scale bar: 1 μm). **i** AFM image of NOA73 surface with a 5 μm-pitch linear corrugation (Scale bar: 4 μm).

To further validate the working principle of the tribocharge-enabled EHDL and its robustness, we repeated the process in a modified setup and checked if the nanovolcanos could still be formed. Specifically, we tried to induce the nanovolcano formation on an NOA73 surface with linear corrugations, instead of the sinusoidal ones formed with the two-beam interference. The preparation steps are shown in Fig. 5.9. First, a PDMS mold was replicated from Ronchi gratings (600 LPMM, MaxLevy; 200 LPMM, Edmund Optics) (Fig. 5.9b). Then the PDMS mold was placed in contact with the spin-coated NOA73 film (Fig. 5.9c) and peeled off after the NOA73 film was partially cured under the broadband UV light (Bluewave 200, Dymax) at 15 mW/cm2 for a preset period of time (Fig. 5.9d) and examined by AFM (Fig. 5.9h and i). Owing to the high oxygen permeability of PDMS and the intrinsic oxygen inhibitory nature of NOA73, the top layer of the NOA73 surface remained fluidic and patternable. In addition, the NOA73 surface was uniformly cured in this scenario since the amplitude of the corrugation (around 60 nm) is much smaller than the thickness of the PDMS mold ($2 \sim 3$ mm). The tribocharged PDMS mold with nanocups was later placed in contact with the partially cured NOA73 surface to induce the tribocharge-enabled EHDL (Fig. 5.9e and f). Upon its complete curing and detachment from the PDMS mold, the NOA73 structure was AFM scanned (Fig. 5.9g). Using samples prepared through such a disparate procedure, we tried to test whether (1) The tribocharge-enabled EHDL works, (2) The UV dose-controlled switching between nanocone and nanovolcano works. Figure 5.10 4 shows the result obtained from the NOA73 surface pre-textured at 1.7 μm pitch. The upper row (a and b) corresponds to lower dose exposure (1.8 J/cm^2) and the lower row (c and d) corresponds to higher dose exposure (2.1 J/cm^2). As emphasized by the dotted circles in Fig. 5.10d, the formation of center dimples and, hence, nanovolcanos occurred only for higher UV dose, higher viscosity case. The trend was repeated in Fig. 5.11 which was obtained from the NOA73 surface pre-textured at a wider, 5.0 μm pitch. Still, the upper row (a and b) corresponds to lower dose exposure (1.35 J/cm2) and the lower row (c and d) corresponds to higher dose exposure (1.8 J/cm^2). The dotted circles in Fig. J/cm^{2}d indicate that the nanovolcano formation occurred only in the higher viscosity sample prepared under higher UV dose.

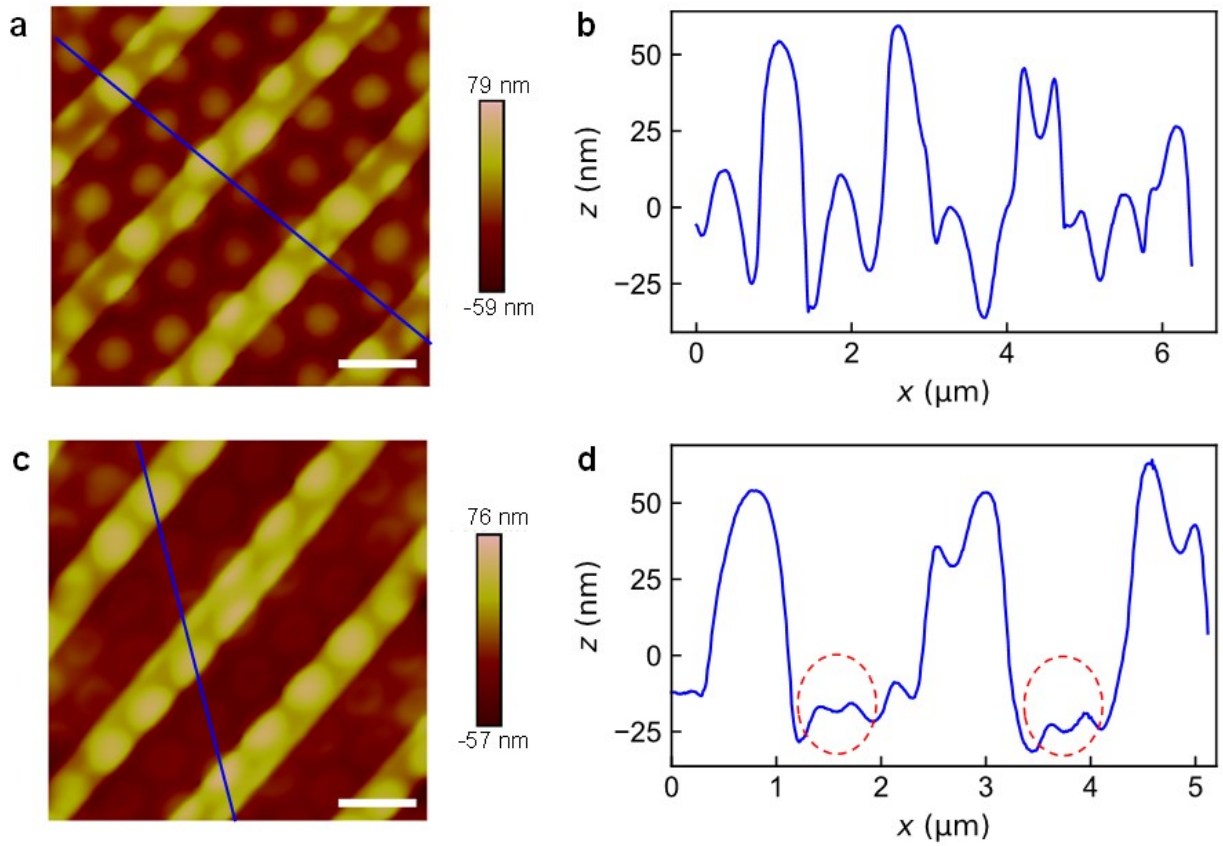

Figure 5.10 Tribo-EHDL on NOA73 surface with a 1.7 μm-pitch linear corrugation **a-d** show the results of performing tribocharge-enabled EHDL on an NOA73 surface textured with replica molding and partial UV curing, rather than the UV laser two-beam interference adopted in the main text. **a**, **b** are made with 120 s exposure under 15 $\mathrm{mW \cdot cm^{-2}}$ intensity, or a dose of 1.8 $\mathrm{mW \cdot cm^{-2}}$. **c**, **d** are made with 140 s exposure under 15 $\mathrm{mW \cdot cm^{-2}}$ intensity, or a dose of 2.1 $\mathrm{mW \cdot cm^{-2}}$. In the trough of **d**, which is more viscous due to the higher dose, the formation of nanovolcano is observed (dotted circles).

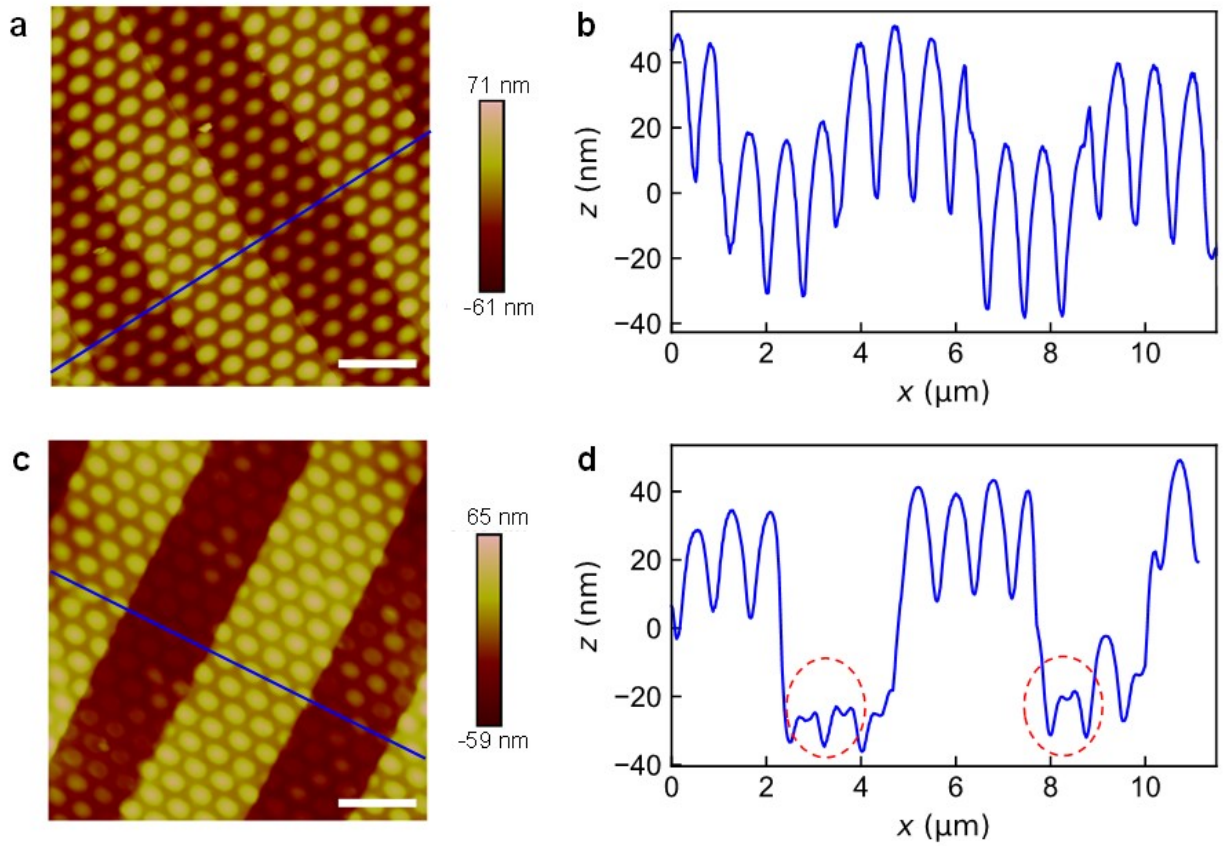

Figure 5.11 Tribo-EHDL on NOA73 surface with 5 μm-pitch linear corrugation **a-d** show the results of performing tribocharge-enabled EHDL on an NOA73 surface textured replica molding and partial UV curing, rather than the UV laser two-beam interference adopted in the main text. **a**, **b** are made with 90 s exposure under 15 mW $\cdot$ cm^{-2} intensity, or a dose of 1.35 J $\cdot$ cm^{-2}. **c**, **d** are made with 120 s exposure under 15 mW $\cdot$ cm^{-2} intensity, or a dose of 1.8 J $\cdot$ cm^{-2}. In the trough of **d**, which is more viscous due to the higher dose, the formation of nanovolcano is observed (dotted circles).

5.5 Shape Control of Nanolens

Inspired from the underfilled crest nanocones in Fig. 5.7f and i, we found that the extent of filling can be well controlled with the applied UV dose before placing the PDMS mold into contact with the NOA film. The modified fabrication process is depicted in Fig. 5.12.

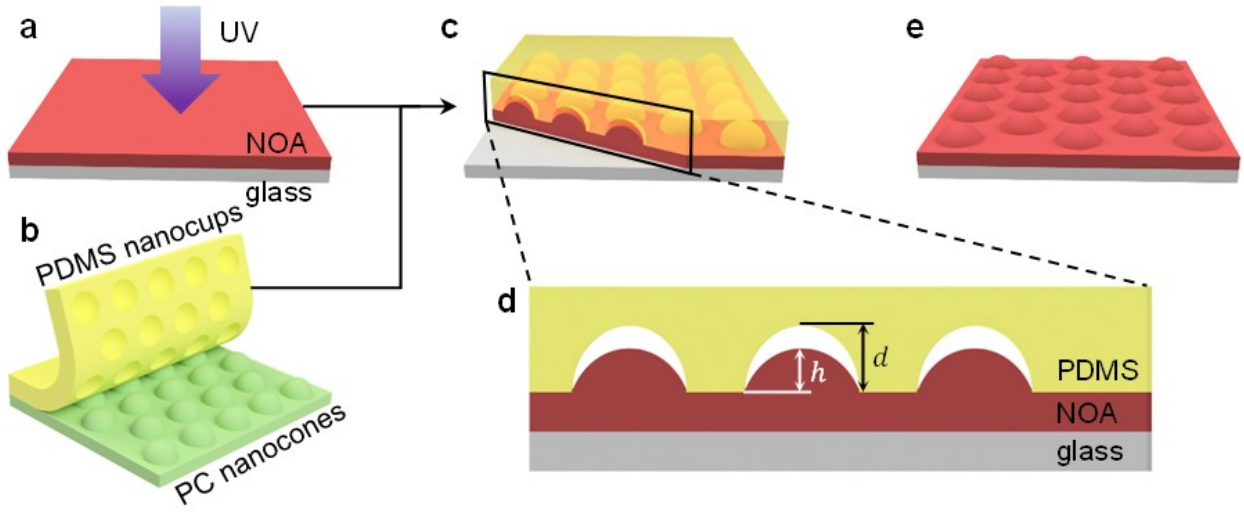

Figure 5.12 Scheme of the fabrication of the curvature-controllable nanolens. (a) Spin–coated NOA film partially cured with UV light. (b) PDMS nanocups replica molded from PC nanocones. (c) The PDMS nanocups in contact with partially cured NOA film. (d) Cross-sectional view showing the underfilling of PDMS nanocups. (e) Curvature-controllable nanolens array.

The UV curable photopolymer (NOA 73, Norland Inc.) was spin coated on a glass substrate and then partially cured by a controlled UV dose (Figure 5.12a). The poly(dimethysiloxane) (PDMS, Sylgard 184) nanocups (period ~750 nm, diameter ~ 500 nm, depth $d \sim 150$ nm), replica molded from the polycarbonate (PC) nanocones array (Figure 5.12b), were placed in contact with the partially cured NOA film (Figure 5.12c). As shown in the cross-sectional view (Figure 5.12d), the PDMS nanocups were underfilled with NOA. The UV dose applied for partial curing determines the extent of filling, and hence, the curvature of nanolenses. The formed NOA nanolenses were then completely cured, resulting in the nanolens array with controllable curvature (Figure 5.12e) after peeling off the PDMS mold. The fabricated nanolens array was then examined with atomic

force microscopy (AFM) in the tapping mode, with the height in the center of nanolens denoted by h (Figure 5.12e).

In Figure 5.13a, the height in the center of nanolenses is plotted over the UV dose applied for partial curing (Figure 5.12a). In the shaded region, the height changes linearly the UV dose, with a slop of $-68.8\text{nm}/(\text{J}/\text{cm}^2)$. With low UV dose applied, the PDMS nanocups were fully filled with NOA, leading to full height NOA nanolenses, as shown in the AFM image (Figure 5.13b). With increasing level of UV dose applied, the height decreases monolithically, as evidenced by the AFM images in Figure 5.13c-e. The same color bar is used to show the difference in height. The corresponding cross-sectional profiles of nanolenses are shown in Figure 5.13f, clearly showing the curvature evolution with increasing level of UV dose applied. The nanolens profiles are fitted to a perfect sphere, showing radii R of 343, 548, 817, and 2813 nm. With geometrical optics, the corresponding f-number, defined as $f/\# = f/D = R/(n-1)/D$, is 1.2, 2.0, 2.9, and 10.0, respectively ($n = 1.56$, refractive index of photopolymer; $D = 500$ nm, base diameter of lens). Although the base diameter of the nanolenses fabricated is around 500 nm, the fabrication can be also extended to microscale, enabling fabrication of microlenses with controllable curvature.

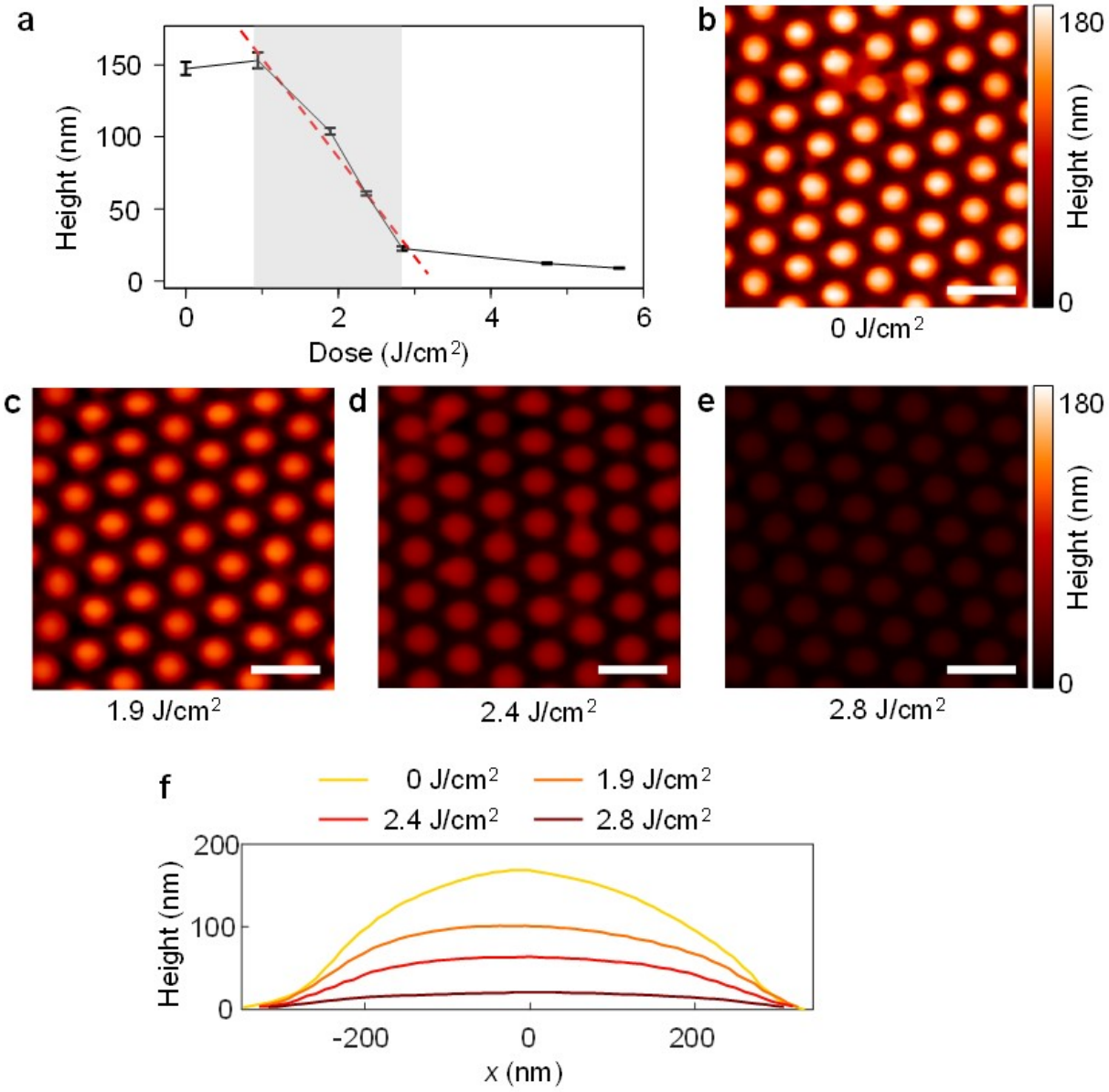

Figure 5.13 (a) Height in the center of nanolenses over the UV dose applied for partial curing. (b) AFM image of full height nanolenses without or low UV dose applied. (c-e) AFM images of nanolenses with decreasing height as a function of the UV dose applied. Scale bars, 1 μm. (f) The cross-sectional profiles of four types of representative nanolenses with different curvatures, corresponding to the AFM images shown in (b)-(e).

CHAPTER 6. CONCLUSIONS AND OUTLOOK

6.1 Summary

In conclusion, we developed a replica molding based technique to produce nanopatterned tribocharges on highly flexible PDMS surfaces capable of forming intimate contact with non-flat surfaces. It is a simple and effective technique which accomplishes both tribocharge generation and patterning in a single operation of replica molding. By generating the charge directly through triboelectrification, this technique also eliminates the need for external supply of electric charge, which often necessitates metallization of the elastomer surface. It also provides well defined targets for the characterization, modeling, and analysis of the nanoscale contact electrification due to its strong nanotexture-dependence.

We then systematically investigated this intriguing phenomenon with a variety of scanning probe microscopic techniques, for example, AFM, KPFM, and EFM, electrostatic modeling, and finite element analysis and established a mechano-triboelectric model. The resulting mechano-triboelectric process model showed that the surface nanotexture controls the tribocharge's distribution pattern by inducing spatially modulated friction during the demolding action. On the basis of the computer simulation results of the demolding action, we identified the tangential sliding distance as the key factor that can be used to predict the tribocharge's final distribution pattern. The model proves remarkably versatile with its prediction range covering all the way down to sub-10 nm scale surface textures with aspect-ratios as low as 0.027. The replica molding-induced CE process itself also proved very useful as a highly scalable technique to create unconventional, complex charge patterns, as evidenced by the ring-, partial eclipse- and dumbbell-shaped charge distributions.

Finally, we integrated the generated nanopatterned surface charge into the EHDL process. In the conventional EHDL, which relies on electric fields generated by patterned electrodes, the polymer either forms an array of nanopillars under the electrode's surface pattern or simply mirrors

the pattern itself through merging of the nanopillars, limiting the feature size to that of the electrode pattern or the characteristic length of the electrohydrodynamic instability. Both are generally at micron-scales. Using the replica molding-induced nanopatterned tribocharges as the source of the electric fields, we have greatly reduced the EHDL's feature size. For instance, this work produced a highly regular array of submicron-scale nanovolcanos by decorating plain nanocones with 10 nm-scale nanocraters. With careful balancing of capillary action and Coulombic attraction, this tribo-electrohydrodynamic lithography will become a versatile tool for fabricating functional materials and meta-surfaces.

6.2 Suggested Future Work

In this dissertation, the morphology of the PET and PC master molds is limited to nanocone, nanocups, and lines. One intriguing future direction is to try other different shapes of master patterns for the replica molding, for example, pyramids and squares. This not only may lead to more interesting charge patterns but also can be used to further test the validity of our mechano-triboelectric model. In addition, instead of replica molding between polymer and polymer, it's also worth trying the contact electrification between semiconductors or metals and polymer. For example, the anisotropically etched silicon pyramids or epitaxially grown copper nanocrystals with multiple facets could be adopted for replica molding with PDMS.

Another future direction is the possible applications of the generated surface charge distribution. Given the highly non-uniform nanopatterned surface charge distribution, one possible application is the self-assembly of nanoparticles, known as nanoxerography [41] or electrostatic assembly [116, 117, 118]. In addition, the longevity of the generated tribocharge should be studied since the replica molding process is very different from the conventional contact electrification, in which completely cured two surfaces are brought into contact and then separated [1]. In our replica molding process, however, one side (PDMS) is in liquid phase in the beginning and then thermally cured and peeled off. The interfacial contact could be more intimate and the physical mechanism might also be different.

Finally, the proposed shape control of nanolens could be extended to cylindrical nanocavities so that the capillary filling can be accurately controlled. Combined with a spatial light modulator for accurate spatiotemporal control of the light distribution, we could develop a grayscale nanoimprinting method capable of printing heterogeneous microscale grains of nanoblocks on the same substrate.

BIBLIOGRAPHY

[1] H. T. Baytekin, A Z Patashinski, M Branicki, Bilge Baytekin, S Soh, and B A Grzybowski. The Mosaic of Surface Charge in Contact Electrification. *Science*, 333(6040):308–312, jul 2011.

[2] Etienne Palleau, Neralagatta M. Sangeetha, Guillaume Viau, Jean Daniel Marty, and Laurence Ressier. Coulomb force directed single and binary assembly of nanoparticles from aqueous dispersions by AFM nanoxerography. *ACS Nano*, 5(5):4228–4235, 2011.

[3] H. O. Jacobs and G. M. Whitesides. Submicrometer Patterning of Charge in Thin-Film Electrets. *Science*, 291(5509):1763–1766, mar 2001.

[4] Lord Kelvin. V. Contact electricity of metals. *The London, Edinburgh, and Dublin Philosophical Magazine and Journal of Science*, 46(278):82–120, jul 1898.

[5] Ning Xi and King Lai. *Nano optoelectronic sensors and devices: nanophotonics from design to manufacturing*. William Andrew, 2011.

[6] Shengming Li, Yusheng Zhou, Yunlong Zi, Gong Zhang, and Zhong Lin Wang. Excluding Contact Electrification in Surface Potential Measurement Using Kelvin Probe Force Microscopy. *ACS Nano*, 10(2):2528–2535, 2016.

[7] Th Glatzel, S. Sadewasser, and M. Ch Lux-Steiner. Amplitude or frequency modulation-detection in Kelvin probe force microscopy. *Applied Surface Science*, 210(1-2 SPEC.):84–89, 2003.

[8] Yu Sheng Zhou, Ying Liu, Guang Zhu, Zong-hong Lin, Caofeng Pan, Qingshen Jing, and Zhong Lin Wang. In Situ Quantitative Study of Nanoscale Triboelectrification and Patterning. *Nano Letters*, 13(6):2771–2776, jun 2013.

[9] K.J. Kwak, S. Yoda, and M. Fujihira. Observation of stretched single DNA molecules by Kelvin probe force microscopy. *Applied Surface Science*, 210(1-2):73–78, mar 2003.

[10] L. Gross, F. Mohn, P. Liljeroth, J. Repp, F. J. Giessibl, and G. Meyer. Measuring the Charge State of an Adatom with Noncontact Atomic Force Microscopy. *Science*, 324(5933):1428–1431, 2009.

[11] C. Riedel, R. Arinero, Ph Tordjeman, M. Ramonda, G. Leveque, G. A. Schwartz, D. G. de Oteyza, A. Alegria, and J. Colmenero. Determination of the nanoscale dielectric constant by means of a double pass method using electrostatic force microscopy. *Journal of Applied Physics*, 106(2):024315, 2009.

[12] S. Barbet, M. Popoff, H. Diesinger, D. Deresmes, D. Théron, and T. Mélin. Cross-talk artefacts in Kelvin probe force microscopy imaging: A comprehensive study. *Journal of Applied Physics*, 115(14):144313, apr 2014.

[13] Johannes Deschler, Johannes Seiler, and Josef Kindersberger. Detection of charges at the interphase of polymeric nanocomposites. *IEEE Transactions on Dielectrics and Electrical Insulation*, 24(2):1027–1037, 2017.

[14] Stephen Y. Chou and Lei Zhuang. Lithographically induced self-assembly of periodic polymer micropillar arrays. *Journal of Vacuum Science & Technology B: Microelectronics and Nanometer Structures*, 17(1999):3197, 1999.

[15] E Schaffer, Thomas Thurn-Albrecht, Thomas P Russell, Ullrich Steiner, Erik Schäffer, Thomas Thurn-Albrecht, and Thomas P Russell. Electrically induced structure formation and pattern transfer. *Nature*, 403(6772):874–877, feb 2000.

[16] J. Lowell and A.C. Rose-Innes. Contact electrification. *Advances in Physics*, 29(6):947–1023, dec 1980.

[17] R. G. Horn and D. T. Smith. Contact Electrification and Adhesion Between Dissimilar Materials. *Science*, 256(5055):362–364, apr 1992.

[18] R. G. Horn, D. T. Smith, and A. Grabbe. Contact electrification induced by monolayer modification of a surface and relation to acid–base interactions. *Nature*, 366(6454):442–443, dec 1993.

[19] Patricia F O'grady. *Thales of Miletus: the beginnings of western science and philosophy*. Taylor & Francis, 2002.

[20] B. A. KWETKUS. PARTICLE TRIBOELECTRIFICATION AND ITS USE IN THE ELECTROSTATIC SEPARATION PROCESS. *Particulate Science and Technology*, 16(1):55–68, jan 1998.

[21] M. Paillet, P. Poncharal, and A. Zahab. Electrostatics of individual single-walled carbon nanotubes investigated by electrostatic force microscopy. *Physical Review Letters*, 94(18):6–9, 2005.

[22] Madhavi Krishnan, Nassiredin Mojarad, Philipp Kukura, and Vahid Sandoghdar. Geometry-induced electrostatic trapping of nanometric objects in a fluid. *Nature*, 467(7316):692–695, 2010.

[23] Jason A. Wiles, Bartosz A. Grzybowski, Adam Winkleman, and George M. Whitesides. A Tool for Studying Contact Electrification in Systems Comprising Metals and Insulating Polymers. *Analytical Chemistry*, 75(18):4859–4867, sep 2003.

[24] Logan S. McCarty, Adam Winkleman, and George M. Whitesides. Ionic Electrets: Electrostatic Charging of Surfaces by Transferring Mobile Ions upon Contact. *Journal of the American Chemical Society*, 129(13):4075–4088, apr 2007.

[25] Logan S. McCarty and George M. Whitesides. Elektrostatische Aufladung durch Separierung von Ionen an Grenzflächen: Kontaktelektrisierung von ionischen Elektreten. *Angewandte Chemie*, 120(12):2218–2239, mar 2008.

[26] R Elsdon and F R G Mitchell. Contact electrification of polymers. *Journal of Physics D: Applied Physics*, 9(10):1445–1460, jul 1976.

[27] Bartosz A. Grzybowski, Adam Winkleman, Jason A. Wiles, Yisroel Brumer, and George M. Whitesides. Electrostatic self-assembly of macroscopic crystals using contact electrification. *Nature Materials*, 2(4):241–245, apr 2003.

[28] Bartosz A. Grzybowski, Marcin Fialkowski, and Jason A. Wiles. Kinetics of Contact Electrification between Metals and Polymers. *The Journal of Physical Chemistry B*, 109(43):20511–20515, nov 2005.

[29] Zhong Lin Wang. Triboelectric Nanogenerators as New Energy Technology for Self-Powered Systems and as Active Mechanical and Chemical Sensors. *ACS Nano*, 7(11):9533–9557, nov 2013.

[30] Zhong Lin Wang, Jun Chen, and Long Lin. Progress in triboelectric nanogenerators as a new energy technology and self-powered sensors. *Energy & Environmental Science*, 8(8):2250–2282, 2015.

[31] Zhong Lin Wang. Triboelectric nanogenerators as new energy technology and self-powered sensors – Principles, problems and perspectives. *Faraday Discuss.*, 176(11):447–458, 2014.

[32] Anyin Li, Yunlong Zi, Hengyu Guo, Zhong Lin Wang, and Facundo M. Fernández. Triboelectric nanogenerators for sensitive nano-coulomb molecular mass spectrometry. *Nature Nanotechnology*, 12(5):481–487, may 2017.

[33] Wei Tang, Jingjing Tian, Qiang Zheng, Lin Yan, Jiangxue Wang, Zhou Li, and Zhong Lin Wang. Implantable Self-Powered Low-Level Laser Cure System for Mouse Embryonic Osteoblasts' Proliferation and Differentiation. *ACS Nano*, 9(8):7867–7873, aug 2015.

[34] Simiao Niu, Xiaofeng Wang, Fang Yi, Yu Sheng Zhou, and Zhong Lin Wang. A universal self-charging system driven by random biomechanical energy for sustainable operation of mobile electronics. *Nature Communications*, 6(1):8975, dec 2015.

[35] Aurelia Chi Wang, Haiyang Zou, Binbin Zhang, Changsheng Wu, Guanlin Liu, Wenbo Ding, Peizhong Feng, Cheng Xu, Zhong Lin Wang, Ming Ma, and Zhiqun Lin. Contact-Electrification between Two Identical Materials: Curvature Effect. *ACS Nano*, 2019.

[36] Mario M. Apodaca, Paul J. Wesson, Kyle J M Bishop, Mark A. Ratner, and Bartosz A. Grzybowski. Contact electrification between identical materials. *Angewandte Chemie - International Edition*, 49(5):946–949, 2010.

[37] Qiang Li, Akshit Peer, In Ho Cho, Rana Biswas, and Jaeyoun Kim. Replica molding-based nanopatterning of tribocharge on elastomer with application to electrohydrodynamic nanolithography. *Nature Communications*, 9(1):974, dec 2018.

[38] Honest Makamba, Jin Ho Kim, Kwanseop Lim, Nokyoung Park, and Jong Hoon Hahn. Surface modification of poly(dimethylsiloxane) microchannels. *Electrophoresis*, 24(21):3607–3619, 2003.

[39] Vincent Linder, Elisabeth Verpoorte, Wolfgang Thormann, N. F. De Rooij, and Hans Sigrist. Surface biopassivation of replicated poly(dimethylsiloxane) microfluidic channels and application to heterogeneous immunoreaction with on-chip fluorescence detection. *Analytical Chemistry*, 73(17):4181–4189, sep 2001.

[40] Gregor Ocvirk, Mark Munroe, Thompson Tang, Richard Oleschuk, Ken Westra, and D. Jed Harrison. Electrokinetic control of fluid flow in native poly(dimethylsiloxane) capillary electrophoresis devices. *Electrophoresis*, 21(1):107–115, 2000.

[41] Heiko O. Jacobs, Stephen A. Campbell, and Michael G. Steward. Approaching nanoxerography: The use of electrostatic forces to position nanoparticles with 100 nm scale resolution. *Advanced Materials*, 14(21):1553–1557, 2002.

[42] Chad R. Barry, Jie Gu, and Heiko O. Jacobs. Charging Process and Coulomb-Force-Directed Printing of Nanoparticles with Sub-100-nm Lateral Resolution. *Nano Letters*, 5(10):2078–2084, oct 2005.

[43] Dan Zhao, Aaron D. Martinez, Xiaolei Xi, Xinlei Ma, Ning Wu, and Tingbing Cao. Self-organization of thin polymer films guided by electrostatic charges on the substrate. *Small*, 7(16):2326–2333, 2011.

[44] A. Born and R. Wiesendanger. Present and future developments of SPM systems as mass storage devices. *Applied Physics A: Materials Science & Processing*, 68(2):131–135, feb 1999.

[45] Shuang Yang Kuang, Guang Zhu, and Zhong Lin Wang. Triboelectrification-Enabled Self-Powered Data Storage. *Advanced Science*, 5(2):1700658, feb 2018.

[46] Yu Sheng Zhou, Sihong Wang, Ya Yang, Guang Zhu, Simiao Niu, Zong-Hong Lin, Ying Liu, and Zhong Lin Wang. Manipulating Nanoscale Contact Electrification by an Applied Electric Field. *Nano Letters*, 14(3):1567–1572, mar 2014.

[47] S. P. Wilks, T. G. G. Maffe\"is, G. T. Owen, K. S. Teng, M. W. Penny, and H. Ferkel. Charge writing on the nanoscale: From nanopatterning to molecular docking. *Journal of Vacuum Science & Technology B: Microelectronics and Nanometer Structures*, 22(4):1995, 2004.

[48] P Mesquida and A Stemmer. Attaching Silica Nanoparticles from Suspension onto Surface Charge Patterns Generated by a Conductive Atomic Force Microscope Tip. *Advanced Materials*, 13(18):1395–1398, sep 2001.

[49] Hiroshi Fudouzi, Mikihiko Kobayashi, and Norio Shinya. Site-Controlled Deposition of Microsized Particles Using an Electrostatic Assembly. *Advanced Materials*, 14(22):1649–1652, nov 2002.

[50] Jang Ung Park, Sangkyu Lee, Sakulsuk Unarunotai, Yugang Sun, Simon Dunham, Taeseup Song, Placid M. Ferreira, Andrew G. Alleyene, Ungyu Paik, and John A. Rogers. Nanoscale, electrified liquid jets for high-resolution printing of charge. *Nano Letters*, 10(2):584–591, 2010.

[51] Dan Zhao, Liting Duan, Mianqi Xue, Wei Ni, and Tingbing Cao. Patterning of electrostatic charge on electrets using hot microcontact printing. *Angewandte Chemie - International Edition*, 48(36):6699–6703, 2009.

[52] Jang-Ung Park, Sangkyu Lee, Sakulsuk Unarunotai, Yugang Sun, Simon Dunham, Taeseup Song, Placid M. Ferreira, Andrew G. Alleyene, Ungyu Paik, and John A. Rogers. Nanoscale, Electrified Liquid Jets for High-Resolution Printing of Charge. *Nano Letters*, 10(2):584–591, feb 2010.

[53] Logan S. McCarty and George M. Whitesides. Electrostatic Charging Due to Separation of Ions at Interfaces: Contact Electrification of Ionic Electrets. *Angewandte Chemie International Edition*, 47(12):2188–2207, mar 2008.

[54] Jesse J. Cole, Chad R. Barry, Robert J. Knuesel, Xinyu Wang, and Heiko O. Jacobs. Nanocontact electrification: Patterned surface charges affecting adhesion, transfer, and printing. *Langmuir*, 27(11):7321–7329, 2011.

[55] H. Dongmo, J. F. Carlotti, G. Bruguier, C. Guasch, J. Bonnet, and J. Gasiot. Electrical characterization of charges in irradiated oxides by electrostatic force microscopy and Kelvin method. *Applied Surface Science*, 212-213(SPEC.):607–613, 2003.

[56] Gerd Binnig, Calvin F Quate, and Ch Gerber. Atomic force microscope. *Physical review letters*, 56(9):930, 1986.

[57] Gerd Binnig, Heinrich Rohrer, Ch Gerber, and Edmund Weibel. Surface studies by scanning tunneling microscopy. *Physical review letters*, 49(1):57, 1982.

[58] M. Nonnenmacher, M. P. O'Boyle, and H. K. Wickramasinghe. Kelvin probe force microscopy. *Applied Physics Letters*, 58(25):2921–2923, jun 1991.

[59] J. M. R. Weaver. High resolution atomic force microscopy potentiometry. *Journal of Vacuum Science & Technology B: Microelectronics and Nanometer Structures*, 9(3):1559, may 1991.

[60] F. Streicher, S. Sadewasser, T. Enzenhofer, H.-W. Schock, and M.Ch. Lux-Steiner. Locally resolved surface photo voltage spectroscopy on Zn-doped CuInS2 polycrystalline thin films. *Thin Solid Films*, 517(7):2349–2352, feb 2009.

[61] Shin'ichi Kitamura, Katsuyuki Suzuki, Masashi Iwatsuki, and C.B Mooney. Atomic-scale variations in contact potential difference on Au/Si(111) 7×7 surface in ultrahigh vacuum. *Applied Surface Science*, 157(4):222–227, apr 2000.

[62] Franck Bocquet, Laurent Nony, Christian Loppacher, and Thilo Glatzel. Analytical approach to the local contact potential difference on (001) ionic surfaces: Implications for Kelvin probe force microscopy. *Physical Review B*, 78(3):035410, jul 2008.

[63] Deyu Li, Yiying Wu, Philip Kim, Li Shi, Peidong Yang, and Arun Majumdar. Thermal conductivity of individual silicon nanowires. *Applied Physics Letters*, 83(14):2934–2936, oct 2003.

[64] J. M. Sturm, A. I. Zinine, H. Wormeester, Bene Poelsema, R. G. Bankras, J. Holleman, and J. Schmitz. Imaging of oxide charges and contact potential difference fluctuations in atomic layer deposited Al2O3 on Si. *Journal of Applied Physics*, 97(6):063709, mar 2005.

[65] Sujit S. Datta, Douglas R. Strachan, E. J. Mele, and A. T. Charlie Johnson. Surface Potentials and Layer Charge Distributions in Few-Layer Graphene Films. *Nano Letters*, 9(1):7–11, jan 2009.

[66] Young-Jun Yu, Yue Zhao, Sunmin Ryu, Louis E. Brus, Kwang S. Kim, and Philip Kim. Tuning the Graphene Work Function by Electric Field Effect. *Nano Letters*, 9(10):3430–3434, oct 2009.

[67] D. Fuertes Marrón, Th. Glatzel, A. Meeder, Th. Schedel-Niedrig, S. Sadewasser, and M. Ch. Lux-Steiner. Electronic structure of secondary phases in Cu-rich CuGaSe2 solar cell devices. *Applied Physics Letters*, 85(17):3755–3757, oct 2004.

[68] B Honig and A Nicholls. Classical electrostatics in biology and chemistry. *Science*, 268(5214):1144–1149, may 1995.

[69] H.G.L. Coster. The Physics of Cell Membranes. *Journal of Biological Physics*, 29(4):363–399, 2003.

[70] F. Sachs, W. E. Brownell, and A. G. Petrov. Membrane Electromechanics in Biology, with a Focus on Hearing. *MRS Bulletin*, 34(9):665–670, sep 2009.

[71] J. Hölzl and F. K. Schulte. Work function of metals. In *Solid surface physics*, pages 1–150. Springer, Berlin, Heidelberg, 1979.

[72] D. El Khoury, R Arinero, J C Laurentie, and J Castellon. Nanoscale surface charge detection in epoxy resin materials using electrostatic force spectroscopy. *AIP Advances*, 6(3):035318, mar 2016.

[73] L. Portes, P. Girard, R. Arinero, and M. Ramonda. Force gradient detection under vacuum on the basis of a double pass method. *Review of Scientific Instruments*, 77(9):096101, 2006.

[74] Laura Fumagalli, Daniel Esteban-Ferrer, Ana Cuervo, Jose L. Carrascosa, and Gabriel Gomila. Label-free identification of single dielectric nanoparticles and viruses with ultraweak polarization forces. *Nature Materials*, 11(9):808–816, sep 2012.

[75] Sascha Sadewasser and Thilo Glatzel, editors. *Kelvin Probe Force Microscopy*, volume 48 of *Springer Series in Surface Sciences*. Springer Berlin Heidelberg, Berlin, Heidelberg, 2012.

[76] Sascha Sadewasser and Thilo Glatzel. *Kelvin Probe Force Microscopy*, volume 65 of *Springer Series in Surface Sciences*. Springer International Publishing, Cham, jun 2018.

[77] Liam Collins, Jason I Kilpatrick, Sergei V Kalinin, and Brian J Rodriguez. Towards nanoscale electrical measurements in liquid by advanced KPFM techniques: a review. *Reports on Progress in Physics*, 81(8):086101, aug 2018.

[78] Yang Jie, Ning Wang, Xia Cao, Ying Xu, Tao Li, Xueji Zhang, and Zhong Lin Wang. Self-Powered Triboelectric Nanosensor with Poly(tetrafluoroethylene) Nanoparticle Arrays for Dopamine Detection. *ACS Nano*, 9(8):8376–8383, 2015.

[79] John David Jackson. *Classical electrodynamics*. John Wiley & Sons, 1999.

[80] Thiago A.L. Burgo, Telma R.D. Ducati, Kelly R. Francisco, Karl J. Clinckspoor, Fernando Galembeck, and Sergio E. Galembeck. Triboelectricity: Macroscopic charge patterns formed by self-arraying ions on polymer surfaces. *Langmuir*, 28(19):7407–7416, 2012.

[81] Nikolaus Knorr. Squeezing out hydrated protons: low-frictional-energy triboelectric insulator charging on a microscopic scale. *AIP Advances*, 1(2):022119, 2011.

[82] Apra Pandey, Jerzy Kieres, and Maciej A. Noras. Verification of non-contacting surface electric potential measurement model using contacting electrostatic voltmeter. *Journal of Electrostatics*, 67(2-3):453–456, may 2009.

[83] A.M. Barnes and A.D. Dinsmore. Heterogeneity of surface potential in contact electrification under ambient conditions: A comparison of pre- and post-contact states. *Journal of Electrostatics*, 81:76–81, jun 2016.

[84] B. D. Terris, J. E. Stern, D. Rugar, and H. J. Mamin. Contact electrification using force microscopy. *Physical Review Letters*, 63(24):2669–2672, 1989.

[85] F Schneider, T Fellner, J Wilde, and U Wallrabe. Mechanical properties of silicones for MEMS. *Journal of Micromechanics and Microengineering*, 18(6):065008, jun 2008.

[86] I D Johnston, D K McCluskey, C K L Tan, and M C Tracey. Mechanical characterization of bulk Sylgard 184 for microfluidics and microengineering. *Journal of Micromechanics and Microengineering*, 24(3):035017, mar 2014.

[87] J.P.M. Hoefnagels, J. Neggers, P.H.M. Timmermans, O. van der Sluis, and M.G.D. Geers. Copper–rubber interface delamination in stretchable electronics. *Scripta Materialia*, 63(8):875–878, oct 2010.

[88] L.C.S. Nunes. Mechanical characterization of hyperelastic polydimethylsiloxane by simple shear test. *Materials Science and Engineering: A*, 528(3):1799–1804, jan 2011.

[89] Clemens Barth, Adam S. Foster, Claude R. Henry, and Alexander L. Shluger. Recent trends in surface characterization and chemistry with high-resolution scanning force methods. *Advanced Materials*, 23(4):477–501, 2011.

[90] Ali Sadeghi, Alexis Baratoff, S. Alireza Ghasemi, Stefan Goedecker, Thilo Glatzel, Shigeki Kawai, and Ernst Meyer. Multiscale approach for simulations of Kelvin probe force microscopy with atomic resolution. *Physical Review B*, 86(7):075407, 2012.

[91] Julia L. Neff and Philipp Rahe. Insights into Kelvin probe force microscopy data of insulator-supported molecules. *Physical Review B - Condensed Matter and Materials Physics*, 91(8):085424, 2015.

[92] Franck Bocquet, Laurent Nony, Christian Loppacher, and Thilo Glatzel. Analytical approach to the local contact potential difference on (001) ionic surfaces: Implications for Kelvin probe force microscopy. *Physical Review B - Condensed Matter and Materials Physics*, 78(3):035410, 2008.

[93] Paru Deshpande, Xiaoyun Sun, and Stephen Y. Chou. Observation of dynamic behavior of lithographically induced self-assembly of supramolecular periodic pillar arrays in a homopolymer film. *Applied Physics Letters*, 79(11):1688–1690, sep 2001.

[94] Paru Deshpande and Stephen Y. Chou. Lithographically induced self-assembly of microstructures with a liquid-filled gap between the mask and polymer surface. *Journal of Vacuum Science & Technology B: Microelectronics and Nanometer Structures*, 19(6):2741, 2001.

[95] Paru Deshpande, Leonard F. Pease, Lei Chen, Stephen Y. Chou, and William B. Russel. Cylindrically symmetric electrohydrodynamic patterning. *Physical Review E*, 70(4):041601, oct 2004.

[96] Ning Wu and William B. Russel. Micro- and nano-patterns created via electrohydrodynamic instabilities. *Nano Today*, 4(2):180–192, 2009.

[97] Stephen Y Chou and Lei Zhuang. Lithographically induced self-construction of polymer microstructures for resistless patterning. *Applied Physics Letters*, 75(7):1004, 1999.

[98] S Harkema and U Steiner. Hierarchical Pattern Formation in Thin Polymer Films Using an Electric Field and Vapor Sorption. *Advanced Functional Materials*, 15(12):2016–2020, dec 2005.

[99] Ning Wu, Leonard F. Pease, and William B. Russel. Toward large-scale alignment of electrohydrodynamic patterning of thin polymer films. *Advanced Functional Materials*, 16(15):1992–1999, 2006.

[100] L. Goldenberg, O. Sakhno, and J. Stumpe. Application of Norland adhesive for holographic recording. *Optical Materials*, 27(8):1379–1385, 2005.

[101] Rhokyun Kwak, Hyun Ha Park, Hangil Ko, Minho Seong, Moon Kyu Kwak, and Hoon Eui Jeong. Partially Cured Photopolymer with Gradient Bingham Plastic Behaviors as a Versatile Deformable Material. *ACS Macro Letters*, 6(5):561–565, 2017.

[102] T. Y. Lee, C. A. Guymon, E. Sonny Jönsson, and C. E. Hoyle. The effect of monomer structure on oxygen inhibition of (meth)acrylates photopolymerization. *Polymer*, 45(18):6155–6162, 2004.

[103] Christian Decker. Kinetic Study and New Applications of UV Radiation Curing. *Macromolecular Rapid Communications*, 23(18):1067–1093, dec 2002.

[104] Hoon Eui Jeong, Rhokyun Kwak, Jae Kwan Kim, and Kahp Y. Suh. Generation and self-replication of monolithic, dual-scale polymer structures by two-step capillary-force lithography. *Small*, 4(11):1913–1918, 2008.

[105] Hans J. Ensikat, Petra Ditsche-Kuru, Christoph Neinhuis, and Wilhelm Barthlott. Superhydrophobicity in perfection: the outstanding properties of the lotus leaf. *Beilstein Journal of Nanotechnology*, 2(1):152–161, mar 2011.

[106] Akshit Peer and Rana Biswas. Extraordinary optical transmission in nanopatterned ultrathin metal films without holes. *Nanoscale*, 8(8):4657–4666, 2016.

[107] Dong Qin, Younan Xia, and George M Whitesides. Soft lithography for micro- and nanoscale patterning. *Nature Protocols*, 5(3):491–502, 2010.

[108] Ying Zhang, Chi Wei Lo, J. Ashley Taylor, and Shu Yang. Replica molding of high-aspect-ratio polymeric nanopillar arrays with high fidelity. *Langmuir*, 22(20):8595–8601, 2006.

[109] Mingfu Zhang, Priyanka Dobriyal, Jiun-Tai Tai Chen, Thomas P. Russell, Jessica Olmo, and Aurora Merry. Wetting Transition in Cylindrical Alumina Nanopores with Polymer Melts. *Nano Letters*, 6(5):1075–1079, may 2006.

[110] Celal Con and Bo Cui. Effect of mold treatment by solvent on PDMS molding into nanoholes. *Nanoscale Research Letters*, 8(1):394, dec 2013.

[111] E Schäffer, T Thurn-Albrecht, T. P Russell, and U Steiner. Electrohydrodynamic instabilities in polymer films. *Europhysics Letters (EPL)*, 53(4):518–524, 2001.

[112] Lin Wu and Stephen Y. Chou. Dynamic modeling and scaling of nanostructure formation in the lithographically induced self-assembly and self-construction. *Applied Physics Letters*, 82(19):3200–3202, may 2003.

[113] Ning Wu and William B. Russel. Dynamics of the formation of polymeric microstructures induced by electrohydrodynamic instability. *Applied Physics Letters*, 86(24):1–3, 2005.

[114] Qingzhen Yang, Ben Q. Li, and Yucheng Ding. A numerical study of nanoscale electrohydrodynamic patterning in a liquid film. *Soft Matter*, 9(12):3412, 2013.

[115] Enoch Kim and George M. Whitesides. Imbibition and Flow of Wetting Liquids in Noncircular Capillaries. *The Journal of Physical Chemistry B*, 101(6):855–863, feb 1997.

[116] E Palleau, N M Sangeetha, and L Ressier. Quantification of the electrostatic forces involved in the directed assembly of colloidal nanoparticles by AFM nanoxerography. *Nanotechnology*, 22(32):325603, aug 2011.

[117] Calum Kinnear, Jasper Cadusch, Heyou Zhang, Jianing Lu, Timothy D. James, Ann Roberts, and Paul Mulvaney. Directed Chemical Assembly of Single and Clustered Nanoparticles with Silanized Templates. *Langmuir*, 34(25):7355–7363, jun 2018.

[118] Daniel Morales, Lauryanne Teulon, Etienne Palleau, Thomas Alnasser, and Laurence Ressier. Single-Step Binary Electrostatic Directed Assembly of Active Nanogels for Smart Concentration-Dependent Encryption. *Langmuir*, 34(4):1557–1563, jan 2018.